Cuenca Gotor, VP.; Gomis, O.; Sans-Tresserras, JÁ.; Manjón Herrera, FJ.; Rodríguez Hernández, P.; Muñoz, A. (2016). Vibrational and elastic properties of As4O6 and As4O6·2He at high pressures: Study of dynamical and mechanical stability. Journal of Applied Physics. 120(15):155901-1-155901-11. doi:10.1063/1.4964875.

Vibrational and elastic properties of As_4O_6 and $As_4O_6 \cdot 2He$ at high pressures: Study of dynamical and mechanical stability

V.P. Cuenca-Gotor,[1] O. Gomis,[2,a)] J.A. Sans,[1] F. J. Manjón,[1]
P. Rodríguez-Hernández,[3] and A. Muñoz [3]

[1] Instituto de Diseño para la Fabricación y Producción Automatizada, MALTA Consolider Team, Universitat Politècnica de València, 46022 València, Spain
[2] Centro de Tecnologías Físicas: Acústica, Materiales y Astrofísica, MALTA Consolider Team, Universitat Politècnica de València, 46022 València, Spain
[3] Departamento de Física, Instituto de Materiales y Nanotecnología, MALTA Consolider Team, Universidad de La Laguna, 38205 Tenerife, Spain
a) Author to whom correspondence should be addressed. Electronic mail: osgohi@fis.upv.es

Abstract

The formation of a new compound with stoichiometry $As_4O_6 \cdot 2He$ at relatively low pressure (3 GPa) has been recently reported when arsenolite (As_4O_6) powder is compressed with helium as a pressure-transmitting medium. In this work, we study the lattice dynamics of As_4O_6 and $As_4O_6 \cdot 2He$ at high pressures from an experimental and theoretical perspective by means of Raman scattering measurements and *ab initio* calculations and report the theoretical elastic properties of both compounds at high pressure. Raman scattering measurements show a completely different behaviour of As_4O_6 and $As_4O_6 \cdot 2He$ at high pressures. Furthermore, the theoretical calculation of phonon dispersion curves and elastic stiffness coefficients at high pressure in both compounds allow us to discuss their dynamical and mechanical stability under hydrostatic compression. Both compounds are dynamically stable even above 20 GPa, but As_4O_6 becomes mechanically unstable at pressures beyond 19.7 GPa. These results allow explaining the pressure-induced amorphization of As_4O_6 found experimentally

above 15-20 GPa and the lack of observation of any instability in $As_4O_6 \cdot 2He$ up to the highest studied pressure (30 GPa).

Keywords: lattice dynamics, elastic properties, high pressure, Raman scattering, *ab initio* calculations
PACS number(s): 31.15.A-, 62.20.-x, 62.50.-p, 71.15.Mb

I. Introduction

Arsenic trioxide (As_2O_3) is a commercially important compound since it is the main precursor to other arsenic compounds, like organoarsenic compounds used in forestry products and pharmaceuticals. The oxide is also used in colorless glass production and in electronics as the precursor to elemental arsenic, arsenic alloys, and arsenide semiconductors **[1]**. Despite the well known toxicity of arsenic, arsenic trioxide has long been of biomedical interest, dating to traditional Chinese medicine, and is still used to treat cancer and other diseases **[2,3]**.

Arsenolite (α-As_2O_3, indeed As_4O_6) is a mineral which is formed by oxidation of As-rich ore deposits as arsenic sulfide or by hydrolysis of arsenic chloride **[4]**. This mineral constitutes the cubic polymorph [space group 227, *Fd-3m*, *Z*=16] of arsenic oxide and is a molecular 3D solid with an open framework structure composed of closed-compact adamantane-type As_4O_6 molecular cages (with strong covalent interatomic As-O bonds) bonded together by weak van der Waals forces and directional intermolecular interactions **[5,6]** [see **Fig. 1(a)**]. In particular, the structure of the As_4O_6 molecular cage can be described by the overlap of four pseudo–tetrahedral units consisting of an As atom surrounded by three O ligands and a cationic lone electron pair (LEP) in such a way that they form a ball with all cation (also anion) LEPs pointing towards the external part of the cage **[7]**.

Apart from the structural characterization of As_4O_6 at high pressures (HP) **[8-10]**, the vibrational properties of arsenolite under compression have been also reported **[11,12]**. In **Ref. 11**, the pressure dependence of all (except one) Raman-active modes were reported as well as the pressure dependence of all infrared (IR)-active modes. Furthermore, additional modes were observed above 6 GPa which were suggested to occur due to a cubic-to-tetragonal phase transition in As_4O_6. However, this phase transition has not been confirmed in the HP structural studies already performed **[8-10]**. Therefore, it is timely to revisit the vibrational properties of As_4O_6 at HP.

Additionally, previous works have reported the structural characterization of As_4O_6 under compression by means of angle dispersive x-ray diffraction (XRD) measurements using different pressure-transmitting media (PTMs) **[8,10]**. In those works it was shown that arsenolite is one of the most compressible non-hydrated minerals. Furthermore, it was shown in several previous works that when this compound is compressed with He, this PTM enters into the largest voids of the structure (16d sites) above 3 GPa to form a stable compound with stoichiometry $As_4O_6{\cdot}2He$ [**Fig. 1(b)**] **[8-10]**. In this regard, it is worth to mention that it has been reported that As_4O_6 undergoes pressure-induced amorphization (PIA) above 15-20 GPa depending on the PTM used **[8,10-12]**; however, it was also shown that $As_4O_6{\cdot}2He$ remained stable at least up to 30 GPa showing no sign of PIA **[8-10]**.

In order to further understand the different behavior of As_4O_6 and $As_4O_6{\cdot}2He$, we study in this work the lattice dynamics of both compounds by means of Raman scattering (RS) measurements at room temperature and *ab initio* calculations of the elastic properties for both compounds at HP. Some thermodynamic properties are also reported in the supplementary material. In this way, we have theoretically studied the dynamical and mechanical stability of As_4O_6 and $As_4O_6{\cdot}2He$ at HP, which allows

explaining prior experimental results. Note that partial results of the lattice dynamics and mechanical stability of both compounds were already reported in **Refs. 8 and 10**.

II. Experimental details

Highly pure arsenolite (As_4O_6) powder (99.999%) was commercially obtained from Sigma Aldrich Company. As_4O_6 powder was loaded together with several ruby balls inside a membrane-type diamond anvil cell (DAC) and was pressurized with different PTM (4:1 metanol-ethanol mixture (MEM) and He) but also without any PTM. The ruby photoluminescence was used for pressure calibration in all measurements **[13]**.

HP-RS measurements at room temperature were performed in a backscattering geometry using a Horiba Jobin-Yvon LabRam HR UV spectrometer in combination with a thermoelectrically-cooled multichannel CCD detector (resolution below 2 cm^{-1}). RS spectra of arsenolite powder were excited either with 532.0 or 632.8 nm laser lines and laser power below 10 mW up to pressures between 12 and 22 GPa. RS measurements were analyzed by fitting Raman peaks with a Voigt profile fixing the Gaussian line width to the experimental setup resolution.

III. Theoretical calculations details

Ab initio total-energy calculations were performed within the density functional theory (DFT) **[14]** using the plane-wave method **[15]** and the pseudopotential theory with the Vienna *ab initio* simulation package (VASP) **[16]** as in a previous work **[10]**. Convergence tests show that in order to have accurate results, the plane wave basis requires an energy cutoff of 520 eV. The integrations in the Brillouin zone were performed using a special k-point sampling, with dense (4x4x4) grid of k-points in order to have high accurate and converged results. Total energies were converged up to

0.001 eV/atom and forces acting on atoms were converged up to 0.003 eV/Å. Exchange and correlation term was computed through PBE for solids prescription **[17]**. In this way, lattice dynamics *ab initio* calculations at the zone center (Γ point) of the Brillouin zone (BZ) were performed using the direct force constant approach **[18]**. To obtain the phonon dispersion curves (PDCs) along high-symmetry directions of the BZ we performed similar calculations using appropriate supercells, which allow the phonon dispersion at k-points to be obtained commensurate with the supercell size **[18]**.

On the other hand, *ab initio* calculations allow the study of the mechanical properties of materials. In particular, the elastic constants describe the mechanical properties of materials in the region of small deformations where the stress-strain relations are still linear. The elastic constants can be obtained by computing the macroscopic stress for a small strain with the use of the stress theorem **[19]**. In the present work, we perform the evaluation of the elastic constants of As_4O_6 and $As_4O_6 \cdot 2He$ with the use of the DFT as implemented in the VASP package **[20].** The ground state and fully relaxed structures were strained in different directions according to their symmetry **[20]**. The total-energy variations were evaluated according to a Taylor expansion for the total energy with respect to the applied strain **[21]**. Due to this fact, it is important to check that the strain used in the calculations guarantees the harmonic behavior. This procedure allows us to obtain the C_{ij} elastic constants in the Voigt notation. The number of independent elastic constants is reduced by crystalline symmetry **[22]**.

IV. Results and Discussion

A. Lattice dynamics

Arsenolite has a primitive unit cell containing two As_4O_6 adamantanoid molecules situated on the T_d sites of the unit cell **[23]**. According to the factor group analysis, arsenolite, as well as senarmontite, has 60 vibrational modes at zone center **[24]**: $\Gamma = 2A_{1g} + 2A_{2u} + 2E_g + 2E_u + 3T_{1g} + 3T_{2u} + 5T_{2g} + 5T_{1u}$, where E and T modes are double and triple degenerated, respectively. In this way, there are nine Raman-active modes: $2A_{1g} + 2E_g + 5T_{2g}$, four IR-active modes: $4T_{1u}$, ten inactive modes: $2A_{2u} + 2E_u + 3T_{1g} + 3T_{2u}$, and one acoustic mode: T_{1u} **[25]**. Most of the above optical modes come from the internal modes of the isolated As_4O_6 molecule: $\Gamma_{vib} = 2A_1 + 2E + 2T_1 + 4T_2$ due to crystal field (or Davydov) splitting **[26]**. From now on, we will add to the optical vibrational modes of a given symmetry a superscript in order of increasing frequency for the sake of clarity.

To date, several studies have been published on arsenolite's Raman spectra at room conditions **[25-30]** and only two at HP **[11,12]**. In the first works there was some disagreement on the assignment of T_{2g} and E_g modes, which has been finally clarified **[26,30]**; however, there remains one E_g vibrational mode yet to be clearly observed and identified **[26,30]**. In the following we will report the pressure dependence of the different Raman-active modes with different PTM and will show the identification of the lost E_g mode.

1. As_4O_6 pressurized with MEM as a PTM

MEM is a good quasi-hydrostatic PTM up to 20 GPa which is not expected to enter into the open framework structure of arsenolite. **Figure 2a** shows the RS spectra of As_4O_6 with MEM as a PTM measured up to 21 GPa. As observed, our RS spectra are similar to those already reported **[11,12]**. **Figure 2b** shows the pressure dependence of the experimental and theoretical Raman-active modes of As_4O_6. Upon compression, several modes shift to upper wavenumbers: the T_{2g}^1 mode at 84 cm^{-1}; the T_{2g}^2 mode at

268 cm^{-1}; the T_{2g}^{3} at 413 cm^{-1}; the A_{1g}^{2} mode at 560 cm^{-1} and the T_{2g}^{5} mode at 780 cm^{-1}. On the other hand, there are a few modes which shift to lower wavenumbers: the E_{g}^{1} mode at 183 cm^{-1}; the A_{1g}^{1} mode at 369 cm^{-1} and the T_{2g}^{4} at 470 cm^{-1}. Due to the closeness of the T_{2g}^{3} and T_{2g}^{4} modes these two modes undergo a phonon anticrossing around 4.5 GPa; i.e., these two modes repel each other at around 4.5 GPa, then the T_{2g}^{3} band gains intensity and shifts to lower wavenumbers, while the T_{2g}^{4} band loses intensity and shifts to upper wavenumbers. Our symmetry assignments performed on the basis of our theoretical calculations agree with those of Grzechnik and Gilliam et al. **[11,30]**. Furthermore, our *ab initio* calculations indicate that there is an E_g mode at 420 cm^{-1}, which is the only Raman-active mode that was not clearly found in previous Raman works. Taking into account that our calculated frequencies underestimate the experimental frequencies, it is expected that the lost E_g mode could be the weak mode near 443 cm^{-1} observed as a shoulder of the intense T_{2g}^{4} mode by Lockwood and Gilliam et al. **[29,30]**. However, we have not observed this mode in RS measurements of As_4O_6 at room conditions or using MEM as a PTM.

Apart from the first-order Raman-active modes, other modes are observed in the RS spectrum of arsenolite as noted by many authors. In particular, we have observed a very weak peak at about 80 cm^{-1} (also seen in **Ref. 11**) close to the T_{2g}^{1} mode at 84 cm^{-1}. In our opinion this extra mode can be tentatively assigned to one of the inactive librational modes, likely T_{1g}^{1}, of the As_4O_6 molecule due to the close similarity of the theoretical frequencies and pressure coefficients of this mode (see **Fig. 2b**), where the theoretical pressure dependence of the two lowest frequency inactive modes is also plotted. We think that this inactive mode could be observed due to local loss of translational periodic conditions in As_4O_6 as pressure increases. Furthermore, with increasing pressure, many Raman modes undergo a progressive asymmetric broadening

resulting in split modes mainly above 10 GPa. These features, which were also noted in **Ref. 11**, are likely caused by the increase of intermolecular interactions; i.e., the increase of interactions among As_4O_6 cages, which finally results in the onset of PIA above 15-20 GPa depending on the PTM used. On the other hand, the reversibility of the changes in the RS spectra above 10 GPa shows little or no hysteresis. We must note that the increase of intermolecular interactions does not result in a reversible phase transition above 6 GPa as suggested by Grzechnik **[11]**. Previous X-ray diffraction measurements confirmed that the cubic symmetry is maintained up to the onset of PIA **[8-10]**. **Table I** summarizes the experimental and theoretical zero-pressure frequencies, pressure coefficients, and derivative of the pressure coefficients for the Raman-active modes of arsenolite. As observed, our results for the Raman-active modes at zero pressure compare well with previous results reported by Grzechnik **[11]** and also with those of Gilliam et al. **[30]** at ambient pressure**.**

For completeness, we have compared the theoretical pressure dependence of the IR-active modes of As_4O_6 with the experimental data taken from **Ref. 11** (see **Fig. S1** in the supplementary material). As observed, there is a rather good agreement between the experimental and theoretical data, so our calculations confirm the four IR-active modes already reported for arsenolite **[11,28]**. The experimental and theoretical zero-pressure frequencies, pressure coefficients, and derivative of the pressure coefficients for the IR-active modes of arsenolite are given in **Table SI** of the supplementary material.

2. As_4O_6 pressurized without any PTM

For a better comparison of our HP-RS measurements on As_4O_6 with those of **Ref. 11**, which were performed with CsI as a PTM, and with those of **Ref. 12** , which were performed without any PTM, we performed measurements without any PTM since arsenolite is a rather good quasi-hydrostatic PTM at low pressures (in fact slightly better

than CsI) **[31]**. RS spectra of As_4O_6 without PTM were measured up to 12 GPa **(Fig. S2** in the supplementary material). A detail of the Raman spectra in the region between 400 and 500 cm^{-1}, where the E_g mode is expected to be observed, is plotted in **Fig. 3a** and the pressure dependence of the frequencies of its Raman-active modes is reported **(Fig. 3b)**. The frequencies and pressure coefficients of the Raman-active modes in As_4O_6 pressurized without any PTM are also shown in **Table I**.

Raman-active modes of As_4O_6 pressurized without any PTM show a similar behaviour with increasing pressure as in the case of As_4O_6 pressurized with MEM as a PTM. However, the width of the Raman-active modes increases with pressure at a much faster rate; i.e., at smaller pressures, than using MEM as a PTM. Curiously, we have found a weak mode near 448 cm^{-1} at room pressure whose pressure dependence is consistent with the theoretical evolution of the E_g^2 mode (see **Figs. 3a, 3b** and **Table I**). Therefore, we have tentatively attributed this weak mode to the lost E_g^2 mode. We have to note that this means that there are three Raman-active modes in the RS of arsenolite in the region from 400 to 500 cm^{-1}. In this respect, previous RS measurements of arsenolite compressed without any PTM already reported three Raman active modes in this region in the RS spectrum at 11 GPa **[12]**. However, this work does not report any analysis of the experimental Raman-active mode frequencies of arsenolite as a function of pressure. We have also to note that the frequency we have found is slightly larger than the one reported by Gilliam et al. **[30]**, but in very good agreement with Hartree-Fock calculations of Jensen et al. **[26]**. At present, we don't know why it has been easier to find this mode under quasi-hydrostatic conditions than under truly hydrostatic conditions (this mode was also not observed when pressurizing with He). We can speculate that the small RS cross section already known for this mode **[26]** can be enhanced by altering selection rules under non-hydrostatic conditions.

3. As_4O_6 pressurized with helium as a PTM

Helium provides the most hydrostatic conditions for HP experiments, but He is so a small atom that it can enter into the cavities of open framework structures present in porous and molecular materials. We have performed a study of As_4O_6 pressurized with He in order to study the effect of He into the compression of this molecular solid. In this regard, we showed in a previous work that He enters into the 16d sites of As_4O_6 and reacts with this molecular solid forming a new compound with stoichiometry $As_4O_6 \cdot 2He$ above 3 GPa **[10]**.

$As_4O_6 \cdot 2He$ has the same cubic structure as As_4O_6 with two formula units per primitive cell. Therefore, according to group theory, $As_4O_6 \cdot 2He$ has 62 vibrational modes at zone center **[24]**: $\Gamma = 2A_{1g} + 2A_{2u} + 2E_g + 2E_u + 3T_{1g} + 3T_{2u} + 5T_{2g} + 7T_{1u}$. In this way, there are nine Raman-active modes: $2A_{1g} + 2E_g + 5T_{2g}$, six IR-active modes: $6T_{1u}$, ten inactive modes: $2A_{2u} + 2E_u + 3T_{1g} + 3T_{2u}$, and one (triply degenerated) acoustic mode: T_{1u}. In summary, there are only two additional IR-active modes in $As_4O_6 \cdot 2He$ than in As_4O_6.

Figure 4a shows the pressure dependence of the RS spectra of As_4O_6 compressed with He up to 3 GPa and of $As_4O_6 \cdot 2He$ from 3 GPa up to 12 GPa. The experimental and theoretical pressure dependence of the different Raman-active modes is presented in **Fig. 4b**. The frequencies and pressure coefficients of the Raman-active modes in $As_4O_6 \cdot 2He$ are shown in **Table II**. As observed, the pressure dependence of Raman-active modes up to 2 GPa follows the same behaviour as As_4O_6 modes studied in previous sections. However, between 2 and 3 GPa many Raman modes undergo a sudden change in frequency. No further sudden change in frequencies is observed above 3 GPa and RS modes from 3 GPa on behave in a different way to Raman-active modes of As_4O_6. Noteworthy, the anticrossing between the two T_{2g} modes, which occurs in

As_4O_6 around 4-5 GPa is retarded up to 11 GPa in $As_4O_6 \cdot 2He$. The good agreement of our experimental and theoretical data in this regard is a clear confirmation of the entrance of He into 16d sites of the arsenolite structure. Since we have not performed IR measurements in $As_4O_6 \cdot 2He$, the pressure dependence of the theoretically IR-active modes of $As_4O_6 \cdot 2He$ is reported in **Fig. S3** in the supplementary material for comparison with future experimental works. As observed, there are two extra IR-active modes in $As_4O_6 \cdot 2He$ between 200 and 300 cm^{-1} whose pressure coefficient is much larger than those coming from As_4O_6.

B. Dynamical stability

To finish the study of the lattice dynamics of As_4O_6 and $As_4O_6 \cdot 2He$ at HP, we report the calculation of PDCs for both compounds at selected pressures which allows the discussion of their dynamical stability under hydrostatic compression **[32]**. **Figure 5** shows the PDCs of As_4O_6 at 0 GPa and 34.7 GPa, while **Fig. 6** shows the PDCs of $As_4O_6 \cdot 2He$ at 5.2 GPa and 35.5 GPa. It can be observed that there is no phonon dispersion relation that undergoes softening to zero frequency on increasing pressure neither in As_4O_6 up to 34.7 GPa nor in $As_4O_6 \cdot 2He$ up to 35.5 GPa. Therefore, we safely conclude that the cubic structure of both compounds is dynamically stable at least up to those pressures.

C. Elastic properties

Since the cubic structures of As_4O_6 and $As_4O_6 \cdot 2He$ belong to the Fd-3m space group, they have point group 4/m -3 2/m, also known as m-3m (or O_h), and belong to the cubic Laue group m-3m (or C I) **[33]** which has three independent second order elastic constants: C_{11}, C_{12}, and C_{44}. When a non-zero uniform stress is applied to the crystal, the elastic properties are described by the elastic stiffness (or stress-strain) coefficients, which are defined as:

$$B_{ijkl} = C_{ijkl} + 1/2\ [\ \delta_{ik}\,\sigma_{jl} + \delta_{jk}\,\sigma_{il} + \delta_{il}\,\sigma_{jk} + \delta_{jl}\,\sigma_{ik} - 2\,\delta_{kl}\,\sigma_{ij}], \quad (1)$$

with C_{ijkl} being the elastic constants evaluated at the current stressed state, σ_{ij} correspond to the external stresses, and δ_{kl} is the Kronecker delta **[34-36].** In the special case of hydrostatic pressure ($\sigma_{11} = \sigma_{22} = \sigma_{33} = -P$) applied to a cubic crystal, the elastic stiffness coefficients in the Voigt notation B_{ij} are: $B_{11} = C_{11} - P$, $B_{12} = C_{12} + P$, and $B_{44} = C_{44} - P$ where P is the hydrostatic pressure. Note that the B_{ij} and C_{ij} are equal at 0 GPa. When the elastic stiffness coefficients B_{ij} are used, all relationships of the elasticity theory can be applied for the crystal under any loading, including Born's stability conditions which are identical in both loaded and unloaded states **[35-39].** **Table III** summarizes the values of the three elastic constants C_{ij} in As_4O_6 and $As_4O_6{\cdot}2He$ at 0 GPa as obtained from our *ab initio* calculations. As observed, C_{11} is larger in $As_4O_6{\cdot}2He$ than in As_4O_6 while C_{12} and C_{44} are smaller in $As_4O_6{\cdot}2He$ than in As_4O_6.

Figure 7 shows the pressure dependence of the elastic constants, C_{ij}, and elastic stiffness coefficients, B_{ij}, in As_4O_6 and $As_4O_6{\cdot}2He$. Despite only B_{ij} are meaningful at any pressure, we report also the pressure dependence of C_{ij} because they are the original magnitudes computed from which B_{ij} are obtained. As observed, C_{11} (and B_{11}) has a larger pressure coefficient in $As_4O_6{\cdot}2He$ than in As_4O_6 while C_{12} (and B_{12}) and C_{44} (and B_{44}) have smaller pressure coefficients in $As_4O_6{\cdot}2He$ than in As_4O_6. Besides, C_{11} (and B_{11}) and C_{12} (and B_{12}) increase with increasing pressure both in As_4O_6 and $As_4O_6{\cdot}2He$ while C_{44} (and B_{44}) tend to saturate with increasing pressure in As_4O_6 but not in $As_4O_6{\cdot}2He$. These results will be discussed later in relation with the mechanical stability of both compounds.

Standard analytical formulas for the bulk (B) and shear (G) moduli in the Voigt **[40]**, Reuss **[41],** and Hill **[42]** approximations, labeled with subscripts V, R, and H, respectively, can be obtained from the set of B_{ij} for any loading in As_4O_6 and $As_4O_6 \cdot 2He$ **[43]:**

$$B_V = B_R = \frac{B_{11} + 2B_{12}}{3} \tag{2}$$

$$B_H = \frac{B_V + B_R}{2} \tag{3}$$

$$G_V = \frac{B_{11} - B_{12} + 3B_{44}}{5} \tag{4}$$

$$G_R = \frac{5(B_{11} - B_{12})B_{44}}{4B_{44} + 3(B_{11} - B_{12})} \tag{5}$$

$$G_H = \frac{G_V + G_R}{2} \tag{6}$$

In the Voigt (Reuss) approximation, uniform strain (stress) is assumed throughout the polycrystal **[40,41]**. Hill has shown that the Voigt and Reuss averages are limits and suggested that the actual effective B and G elastic moduli can be approximated by the arithmetic mean of the two bounds **[42]**. The Young (E) modulus and the Poisson's ratio (ν) are calculated with the expressions **[44,45]**:

$$E_X = \frac{9B_X G_X}{G_X + 3B_X} \tag{7}$$

$$\nu_X = \frac{1}{2}\left(\frac{3B_X - 2G_X}{3B_X + G_X}\right) \tag{8}$$

where the subscript X refers to the symbols V, R, and H. In this work we report the elastic moduli in the Hill approximation. We summarize in **Table III** all the values obtained for B_H, G_H, and E_H in As_4O_6 and $As_4O_6 \cdot 2He$ at 0 GPa. Note that our calculated

value for the bulk modulus in the Hill approximation is 9.8 (9.2) GPa for As_4O_6 ($As_4O_6 \cdot 2He$); which is in rather good agreement with the value of B_0= 7.6 (6.4) GPa obtained from our PBEsol structural calculations via a fit to a third-order Birch Murnaghan equation of state **[8,10]** and with those of Birch-Murnaghan EoS fit to p(V) data computed within the PAW_PBE-D2 approach in Ref. **[9]**. Furthermore, both values are comparable to experimental values of B_0= 7(2) GPa and 4(2) GPa obtained via a fit to a third-order Birch Murnaghan equation of state for As_4O_6 and $As_4O_6 \cdot 2He$, respectively **[8,10]**. Note that the bulk modulus of $As_4O_6 \cdot 2He$ at zero pressure was extrapolated from data above 3 GPa since this compound is not stable below this pressure.

The above results give us confidence about the correctness of our elastic constants calculations. With this subject in mind, we have compared the bulk modulus and shear modulus in both compounds, which is indicative of the difference between the elastic behavior of both compounds. In As_4O_6 the bulk modulus is larger than the shear modulus, while in $As_4O_6 \cdot 2He$ the contrary is observed. This means that As_4O_6 is more resistive to compression than to shear stresses while the contrary is observed in $As_4O_6 \cdot 2He$.

Table III also includes the values of the Poisson's ratio (v_H), the ratio between the bulk and shear modulus, B_H/G_H, and the Zener elastic anisotropy factor A at 0 GPa for both compounds. The Poisson's ratio provides information about the characteristics of the bonding forces and chemical bonding. The value of the Poisson's ratio in the Hill approximation is v = 0.14 (0.08) in As_4O_6 ($As_4O_6 \cdot 2He$). This value indicates that the interatomic bonding forces are predominantly non central ($v < 0.25$) and that directional intramolecular and intermolecular bonding is predominant at 0 GPa **[5,46,47].**

The B_H/G_H ratio is a simple relationship given by Pugh **[48]**, empirically linking the plastic properties of a material with its elastic moduli. According to the Pugh criterion, a high B_H/G_H ratio is associated with ductility, whereas a low ratio corresponds to brittleness. The critical value for the B_H/G_H ratio is around 1.75, which separates ductile and brittle materials. In our study, we have found values of B/G at 0 GPa below 1.75 for As_4O_6 and $As_4O_6{\cdot}2He$. Therefore, both compounds are fragile at zero pressure, being $As_4O_6{\cdot}2He$ more fragile than As_4O_6.

One of the elastic properties of crystals with more importance for both engineering science and crystal physics is the elastic anisotropy, because it is highly correlated to the possibility of inducing microcraks in materials **[49]**. This anisotropy can be quantified with the Zener anisotropy factor A, which is defined as $A=2B_{44}/(B_{11}-B_{12})$. If A is equal to 1, no anisotropy exists. On the other hand, the more this parameter differs from 1 the more elastically anisotropic is the crystalline structure. The value of A for As_4O_6 is closer to 1 than for the case of $As_4O_6{\cdot}2He$. Therefore, the latter is more elastically anisotropic than the former at 0 GPa.

Figures 8 and 9 show the pressure dependence of B, G, and E elastic moduli, ν Poisson's ratio, B/G ratio and Zener anisotropy, A, in As_4O_6 and $As_4O_6{\cdot}2He$. It can be noted that the Hill bulk modulus, B_H, increases with pressure reaching a maximum value close to 115 GPa in both compounds at 20 GPa. Contrarily, the G_H and E_H moduli increase with pressure up to 9 GPa in As_4O_6 and decrease for larger pressures. This behavior is different to that of $As_4O_6{\cdot}2He$ where both G_H and E_H increase with pressure up to the maximum calculated pressure (35.5 GPa).

On the other hand, the Poisson's ratio shows a curious pressure dependence in both compounds. It strongly increases with pressure up to 2 GPa and then tends to saturate above this pressure. It reaches a value of 0.46 (0.32) at 20 GPa for As_4O_6

($As_4O_6 \cdot 2He$). These values indicate an increment of the ductility and of the metallic behavior; i.e., the progressive loss of interatomic bond directionality, with increasing pressure in both compounds. It must be stressed that the approximation of the Poisson's ratio of As_4O_6 to 0.5 (superior limit of the Poisson's ratio) near 20 GPa is likely due to the tendency of As_4O_6 towards a mechanical instability **[47]**. Note that the *B/G* ratio, which is related to the Poisson's ratio **[47]**, also increases with pressure in the two compounds; however the increase is moderate in $As_4O_6 \cdot 2He$ and abrupt in As_4O_6 above 10 GPa; thus suggesting the presence of a mechanical instability in this later compound. Finally, the Zener anisotropy factor also shows a quite different behavior in both compounds. It increases considerably in As_4O_6 especially above 10 GPa while it stays nearly constant (around 0.6) in $As_4O_6 \cdot 2He$. Again, these results indicate that the elastic anisotropy strongly increases in As_4O_6 with pressure, but it remains constant in $As_4O_6 \cdot 2He$. Therefore, the strong increase of the elastic anisotropy in As_4O_6 with pressure could be also understood as a signal of a mechanical instability in arsenolite at high pressure.

One of the most common elastic properties and less easy to handle is hardness, which is a property generally related to both the elastic and plastic properties of a material. Hardness is an unusual physical property because it is not an intrinsic materials property, but the result of a defined measurement procedure susceptible to precise definitions in terms of fundamental units of mass, length, and time. In practice, hardness is measured by the size of the indentation made on a specimen by a load of a specified shape when a force is applied during a certain time. In this way, there are three principal standard methods for expressing the relationship between hardness and the size of the indentation, these being Brinell, Rockwell, and Vickers. The Vickers hardness, H_v, can be calculated by the formula proposed by Tian et al. **[50]**:

$$H_v = 0.92(G/B)^{1.137} G^{0.708} \quad (9)$$

We used this formula as it eliminates the possibility of unrealistic negative hardness. The values of H_v for As_4O_6 and $As_4O_6 \cdot 2He$ at 0 GPa are included in **Table III**. As observed, $As_4O_6 \cdot 2He$ is harder than As_4O_6 and both have values of H_v are approximately between 4-6 GPa at 0 GPa when using elastic moduli in the Hill approximation. Since H_v at 0 GPa is smaller than 10 GPa, both compounds can be classified as relatively soft materials.

Figure 10 shows the pressure evolution of the Vickers hardness with pressure. It is observed that H_v decreases as pressure increases for both oxides. This is related to the fact that the B/*G* ratio increases with pressure. In this way, both compounds become softer as pressure increases in good agreement with the increase of their ductility (*B*/*G* ratio) as stated above. We note that H_v for $As_4O_6 \cdot 2He$ decreases notably with pressure approaching 0 GPa at 20 GPa.

Finally, one elastic property which is fundamental for Earth Sciences in order to interpret seismic waves is the average sound velocity, v_m **[51]**. In polycrystalline materials v_m is given by **[52]**:

$$v_m = \left[\frac{1}{3} \left(\frac{2}{v_{trans}^3} + \frac{1}{v_{lon}^3} \right) \right]^{-1/3} \quad (10)$$

where v_{trans} and v_{lon} are the transverse and longitudinal elastic wave velocities of the polycrystalline material which are given by:

$$v_{lon} = \left(\frac{B + \frac{4}{3} G}{\rho} \right)^{1/2} \quad (11)$$

$$v_{trans} = \left(\frac{G}{\rho} \right)^{1/2} \quad (12)$$

where B and G are the elastic moduli and ρ the density. Values of the density and wave velocities v_m, v_{lon} and v_{trans} at 0 GPa are given for both oxides in **Table III**. Wave velocities are greater for $As_4O_6 \cdot 2He$ than for As_4O_6 because of the higher value of the shear modulus G in the former than in the later and the slightly smaller density of the former than in the later.

Figure 11 reports the evolution with pressure of the elastic wave velocities for both oxides. Using elastic moduli in the Hill approximation, the calculated v_{lon} increases with pressure reaching a value larger than 4725 m/s (5580 m/s) at 20 GPa in As_4O_6 ($As_4O_6 \cdot 2He$). A similar behavior is observed for velocities v_{trans} and v_m in $As_4O_6 \cdot 2He$. However, the corresponding velocities v_{trans} and v_m increase in As_4O_6 reaching a maximum value around 6 GPa and decrease above this pressure.

In order to finish this section, where different magnitudes derived from the elastic constants have been obtained and analysed, we refer the reader to the supplementary material in order to get information on a few thermodynamic properties (Debye temperature and minimum thermal conductivity) obtained for As_4O_6 and $As_4O_6 \cdot 2He$.

D. Mechanical stability

To finish this work, we study the mechanical stability of the cubic structure in As_4O_6 and $As_4O_6 \cdot 2He$ at HP. For that purpose, we make use of the elastic stiffness coefficients reported in the previous section. The mechanical stability of a crystal at zero pressure can be studied with the Born stability criteria **[53]**. However, the study of the mechanical stability of a crystal at HP requires the generalization of the Born

stability criteria to the case when an external load is applied **[54-56]**. These generalized stability criteria for cubic crystals with three independent elastic constants are given by the following conditions:

$$M_1 = B_{11} + 2B_{12} > 0 \quad (13)$$

$$M_2 = B_{11} - B_{12} > 0 \quad (14)$$

$$M_3 = B_{44} > 0. \quad (15)$$

where B_{11}, B_{12}, and B_{44} are the elastic stiffness coefficients at the considered pressure. These generalized stability criteria are plotted in **Fig. 12**. It is found that **Eq. (14)**, called the Born instability **[55]**, is violated at 19.7 GPa in As_4O_6; however, none of the three generalized stability criteria is violated in $As_4O_6 \cdot 2He$ up to 35.5 GPa. Therefore, our theoretical study of the mechanical stability suggests that the cubic structure of As_4O_6 becomes mechanically unstable beyond 19.7 GPa, in good agreement with the observation of PIA in the pressure range between 15 and 20 GPa depending on the PTM used **[8,10-12]**. On the other hand, our calculations show that there is no mechanical instability of $As_4O_6 \cdot 2He$ up to 35.5 GPa, in good agreement with the observation of the cubic phase of this new compound up to 30 GPa **[8,10]**. Finally, it must be noted that our theoretical results on the mechanical instability of As_4O_6 above 19.7 GPa do not agree with results on single crystals of As_4O_6 pressurized with He, where He partially entered into the pores of As_4O_6 **[9]**.

IV. **Concluding Remarks**

We have experimentally and theoretically studied the lattice dynamics of As_4O_6 and $As_4O_6 \cdot 2He$ at HP and found a different HP behavior in the Raman-active modes of both compounds which support the inclusion of He into 16d sites of the arsenolite

structure above 2-3 GPa. On the other hand, we have studied the dynamical stability of the cubic structure of both compounds and it has been found that As_4O_6 and $As_4O_6 \cdot 2He$ are dynamically stable at least up to 34.7 and 35.5 GPa, respectively.

Additionally, we have theoretically studied the elastic and thermodynamic behavior of both compounds at HP. It has been found that most of the properties of both compounds are similar at low pressures. The elastic constants and the elastic stiffness coefficients increase with increasing pressure in all the pressure range; however, the pressure coefficients of the elastic stiffness coefficients B_{11} and B_{12} are quite different in both compounds, thus resulting in a completely different HP behavior of shear and Young moduli, *B/G* ratio, Poisson's ratio, Vickers hardness and Zener anisotropy in both compounds. In this context, both compounds are more resistive to volume compression than to shear deformation ($B > G$) at all pressures. The average elastic wave velocity, Debye temperature and minimum thermal conductivity of both compounds are also similar at low pressures, but show a different behavior at HP. From the behavior of the elastic stiffness coefficients at HP we have studied the mechanical stability of the cubic structure at HP in both compounds and have found that the cubic structure becomes mechanically unstable at 19.7 GPa in As_4O_6, while there is no mechanical instability in $As_4O_6 \cdot 2He$ at least up to 35.5 GPa. These results are in good agreement with experiments which show PIA in As_4O_6 above 15-20 GPa (depending on the PTM used) and with the experimental observation of the cubic structure of $As_4O_6 \cdot 2He$ up to 30 GPa without signs of PIA.

Supplementary material

See supplementary material for IR-active modes and thermodynamic properties in As_4O_6 and $As_4O_6 \cdot 2He$ along with the Raman scattering spectra of arsenolite at selected pressures without any PTM.

Acknowledgments

This study is supported by the Spanish Ministerio de Economía y Competitividad under projects MAT2013-46649-C4-2-P/3-P and MAT2015-71070-REDC. A.M. and P.R-H. acknowledge computing time provided by Red Española de Supercomputación (RES) and MALTA-Cluster.

References

[1] S. C. Grund, K. Hanusch, and H. Wolf. Arsenic and Arsenic Compounds in *Ullmann's Encyclopedia of Industrial Chemistry* (Wiley-VCH, 2005). doi:10.1002/14356007.a03_113.pub2

[2] M. Gielen, and E. R. Tiekink. *Metallotherapeutic Drugs and Metal-Based Diagnostic Agents.* (John Wiley & Sons, 2005) p. 298.

[3] J. Liu, Y. Lu, Q. Wu, R. A. Goyer, and M. P. Waalkes, J. Pharmacol. Exp. Therap. 326, 363 (2008).

[4] G. Brauer. *Handbook of Preparative Inorganic Chemistry* (Academic Press, 1963).

[5] G. V. Gibbs, A. F. Wallace, D. F. Cox, P. M. Dove, R. T. Downs, N. L. Ross, and K. M. Rosso, J. Phys. Chem. A 113, 736 (2009).

[6] P. A. Gunka, Z. Gontarz and J. Zachara, Phys. Chem. Chem. Phys. 17, 11020 (2015).

[7] F. Pertlik, Czech. J. Phys. B 28, 170 (1978).

[8] J.A. Sans, F.J. Manjón, C. Popescu, V.P. Cuenca-Gotor, O. Gomis, A. Muñoz, P. Rodríguez-Hernández, J. Pellicer-Porres, A.L.J. Pereira, D. Santamaría-Pérez, and A. Segura, arxiv: 1502.04279.

[9] P. A. Gunka, K. F. Dziubek, A. Gladysiak, M. Dranka, J. Piechota, M. Hanfland, A. Katrusiak, and J. Zachara, Cryst. Growth Des. 15, 3740 (2015).

[10] J.A. Sans, F.J. Manjón, C. Popescu, V.P. Cuenca-Gotor, O. Gomis, A. Muñoz, P. Rodríguez-Hernández, J. Contreras-García, J. Pellicer-Porres, A.L.J. Pereira, D. Santamaría-Pérez, and A. Segura, Phys. Rev. B 93, 054102 (2016).

[11] A. Grzechnik, J. Solid State Chem. 144, 416 (1999).

[12] E. Soignard, S.A. Amin, Q. Mei, C.J. Benmore, and J.L. Yarger, Phys. Rev. B 77, 144113 (2008).

[13] H. K. Mao, J. Xu, and P. M. Bell, J. Geophys. Res. 91, 4673 (1986).

[14] P. Hohenberg and W. Kohn, Phys. Rev. 136, 3864 (1964).

[15] P. E. Blochl, Phys. Rev. B 50, 17953 (1994).

[16] G. Kresse and J. Hafner, Phys. Rev. B 47, 558 (1993); 49, 14251 (1994); G. Kresse and J. Furthmüller, Comput. Mater. Sci. 6, 15 (1996); Phys. Rev. B 54, 11169 (1996).

[17] J. P. Perdew, A. Ruzsinszky, G. I. Csonka, O. A. Vydrow, G. E. Scuseria, L. A. Constantin, X. Zhou, and K. Burke, Phys. Rev. Lett. 100, 136406 (2009).

[18] K. Parlinski, Z. Q. Li, and Y. Kawazoe, Phys. Rev. Lett. 78, 4063 (1997).

[19] N. Chetty, A. Muñoz, and R. M. Martin, Phys. Rev. B. 40, 11934 (1989).

[20] Y. Le Page and P. Saxe, Phys. Rev. B. 65, 104104 (2002).

[21] O. Beckstein, J. E. Klepeis, G. L. W. Hart, and O. Pankratov, Phys. Rev. B 63, 134112 (2001).

[22] J. F. Nye, *Physical Properties of Crystals. Their Representation by Tensor and Matrices* (Oxford University Press, 1957).

[23] P. Ballirano and A. Maras, Z. Kristallogr. NCS 217, 177 (2002).

[24] E. Kroumova, M.I. Aroyo, J.M. Perez-Mato, A. Kirov, C. Capillas, S. Ivantchev, and H. Wondratschek, Phase Trans. 76, 155 (2003).

[25] I.R. Beattie, K.M.S. Livingston, G. A. Ozin, and D.J. Reynolds, J. Chem. soc. A 449 (1970).

[26] J. O. Jensen, S. J. Gilliam, A. Banerjee, D. Zeroka, S. J. Kirkby, and C. N. Merrow, J. Mol. Str.: THEOCHEM 664-665, 145 (2003).

[27] H.A. Szymansky, L. Marabella, J. Hoke, and J. Harter, Appl. Spectros. 22, 297 (1968).

[28] S.B. Brumbach and G.M. Rosenblatt, J. Chem. Phys. 56, 3110 (1972).

[29] D.J. Lockwood, J. Sol. Chem. 29, 1039 (2000).

[30] S. J. Gilliam, C. N. Merrow, S. J. Kirkby, J. O. Jensen, D. Zeroka and A. Banerjee, J. Solid State Chem. 173, 54 (2003).

[31] J.A. Sans, F.J. Manjón, C. Popescu, A. Muñoz, P. Rodríguez-Hernández, J.L. Jordá, and F. Rey, J. Phys: Condens. Matter 28, 475403 (2016).

[32] M. Born, Proc. Cambridge Philos. Soc. 36, 160 (1940).

[33] J.D. Clayton, Nonlinear Mechanics of Crystals, Solid Mechanics and Its Applications 177 (Springer, New York, 2010).

[34] D. C. Wallace, "Thermoelastic theory of stressed crystals and higher-order elastic constants," in *Solid State Physics*, edited by F. S. Henry Ehrenreich, D. Turnbull, and F. Seitz (Academic Press, 1970), vol. 25, pp. 301–404.

[35] J. Wang, S. Yip, S. R. Phillpot, and D. Wolf, Phys. Rev. Lett. 71, 4182 (1993).

[36] J. Wang, J. Li, S. Yip, S. Phillpot and D. Wolf, Phys. Rev. B 52, 12627 (1995).

[37] Z. Zhou and B. Joós, Phys. Rev. B 54, 3841 (1996).

[38] B. B. Karki, L. Stixrude, and R. M. Wentzcovitch, Reviews of Geophysics 39, 507 (2001).

[39] O. M. Krasil'nikov, M. P. Belov, A. V. Lugovskoy, I. Yu. Mosyagin, and Yu. Kh. Vekilov, Computational Materials Science 81, 313 (2014).
[40] W. Voigt, *Lehrbuch der Kristallphysik* (B. G. Teubner, Leipzig, Germany, 1928).
[41] A. Reuss, Z. Angew, Math. Mech. 9, 49 (1929).
[42] R. Hill, Proc. Phys. Soc. London A 65, 349 (1952).
[43] O. Gomis, D. Santamaría-Pérez, J. Ruiz-Fuertes, J. A. Sans, R. Vilaplana, H. M. Ortiz, B. García-Domene, F. J. Manjón, D. Errandonea, P. Rodríguez-Hernández, A. Muñoz, and M. Mollar, J. Appl. Phys. 116, 133521 (2014).
[44] R. Caracas and T. B. Ballaran, Phys. Earth Planet. Int. 181, 21 (2010).
[45] Q. J. Liu, Z. T. Liu, and L. P. Feng, Commun. Theor. Phys. 56, 779 (2011).
[46] V. V. Brazhkin, A. G. Lyapin, and R. J. Hemley, Philos. Mag. A 82, 231 (2002).
[47] G. N. Greaves, A. L. Greer, R. S. Lakes, and T. Rouxel, Nat. Mater. 10, 823 (2011).
[48] S. F. Pugh, Philos. Mag. 45, 823 (1954).
[49] V. Tvergaard and J. W. Hutchinson, J. Am. Ceram. Soc. 71, 157 (1988).
[50] Y. Tian, B. Xu, and Z. Zhao, Int. J. Refract. Met. H. 33, 93 (2012).
[51] J. P. Poirier, *Introduction to the Physics of the Earth's Interior* (Cambridge University Press, 2000).
[52] O. L. Anderson, J. Phys. Chem. Solids 24, 909 (1963).
[53] M. Born and K. Huang, *Dynamical Theory of Crystal Lattices* (Oxford University Press, 1954) p. 140.
[54] D.C. Wallace, Phys. Rev. 162, 776 (1967).
[55] G. Grimvall, B. Magyari-Köpe, V. Ozolinš, and K. A. Persson, Rev. Mod. Phys. 84, 945 (2012).
[56] H. Wang and M. Li, J. Phys. Condens. Matter 24, 245402 (2012).

Table I. Experimental and theoretical frequencies and pressure coefficients of Raman-active (R) modes in As_4O_6 at 0 GPa. The inactive modes $T_{2u}{}^1$ and $T_{1g}{}^1$ are also included.

	Ab initio calculations		Experiments					
Mode (Sym)	ω_0 (cm^{-1})	$\frac{\partial\omega}{\partial P}$ $\left(\frac{cm^{-1}}{GPa}\right)$	ω_0^a (cm^{-1})	$\frac{\partial\omega^a}{\partial P}$ $\left(\frac{cm^{-1}}{GPa}\right)$	ω_0^b (cm^{-1})	$\frac{\partial\omega^b}{\partial P}$ $\left(\frac{cm^{-1}}{GPa}\right)$	ω_0^c (cm^{-1})	$\frac{\partial\omega^c}{\partial P}$ $\left(\frac{cm^{-1}}{GPa}\right)$
$T_{2u}{}^1$	70.7	11.9						
$T_{1g}{}^1$	81.8	7.8	85.5	6.0	82.3	8.9		
$T_{2g}{}^1$ (R)	82.1	15.2	84.7	12.9	83.8	13.2	81.0	10.0
$E_g{}^1$ (R)	168.0	-2.5	182.5	-2.3	182.6	-2.0	181.1	-1.0
$T_{2g}{}^2$ (R)	249.4	6.4	267.5	4.9	267.1	5.0	265.2	3.9
$A_{1g}{}^1$ (R)	353.4	-5.7	368.6	-3.6	368.7	-3.0	367.2	-2.0
$T_{2g}{}^3$ (R)	385.4	16.0	413.4	11.8	413.2	11.6	410.6	10.0
$E_g{}^2$ (R)	418.9	-10.4			449.2	-6.4		
$T_{2g}{}^4$ (R)	448.5	-8.7	470.3	-5.6	470.5	-5.1	469.8	-3.0
$A_{1g}{}^2$ (R)	524.6	0.5	559.4	1.7	559.3	2.0	558.8	1.4
$T_{2g}{}^5$ (R)	747.9	-3.7	780.0	-1.5	780.5	-2.3	780.5	-0.6

[a] Experiment with MEM.

[b] Experiment without any PTM.

[c] Experiment with CsI (data from Ref. 11).

Table II. Experimental and theoretical frequencies and pressure coefficients of Raman-active (R) modes in $As_4O_6 \cdot 2He$ at 3 GPa. The inactive mode $T_{1g}^{\ 1}$ is also included.

	Ab initio calculations		Experiments	
Mode (Sym)	ω_0 (cm^{-1})	$\frac{\partial\omega}{\partial P}$ $\left(\frac{cm^{-1}}{GPa}\right)$	ω_0 (cm^{-1})	$\frac{\partial\omega}{\partial P}$ $\left(\frac{cm^{-1}}{GPa}\right)$
$T_{1g}^{\ 1}$	98.9	2.3	102.0	3.6
$T_{2g}^{\ 1}$ (R)	108.2	6.6	108.8	6.7
$E_g^{\ 1}$ (R)	168.7	-0.3	183.1	0.4
$T_{2g}^{\ 2}$ (R)	244.3	10.0	276.4	3.3
$A_{1g}^{\ 1}$ (R)	349.7	-4.9	369.8	-0.3
$T_{2g}^{\ 3}$ (R)	412.3	-0.7	435.0	-1.3
$E_g^{\ 2}$ (R)	409.2	-5.9		
$T_{2g}^{\ 4}$ (R)	448.7	-2.4	469.7	3.7
$A_{1g}^{\ 2}$ (R)	528.8	1.8	565.7	2.2
$T_{2g}^{\ 5}$ (R)	754.7	2.2	788.6	2.0

Table III. C_{ij} elastic constants (in GPa) for As_4O_6 and $As_4O_6 \cdot 2He$ at 0 GPa. Elastic moduli B_H, G_H, and E_H (in GPa), Possion's ratio (ν_H) given in the Hill approximation, labeled with subscript H in As_4O_6 and $As_4O_6 \cdot 2He$ at 0 GPa. The B_H/G_H ratio, Zener anisotropy factor (A), Vickers hardness (H_v in GPa), density (ρ in g/cm^3), and longitudinal (v_{lon}), transverse (v_{trans}) and averaged (v_m) elastic wave velocities (all in m/s) are also included.

	As_4O_6	$As_4O_6 \cdot 2He$
C_{11}	21.2	28.8
C_{12}	4.0	-0.6
C_{44}	9.8	8.7
B_H	9.8	9.2
G_H	9.3	10.7
E_H	21.2	23.1
ν_H	0.14	0.08
B_H/G_H	1.05	0.86
A	1.15	0.59
H_v	4.2	5.8
P	3.982	3.766
v_{lon}	2359.8	2495.3
v_{trans}	1529.6	1684.1
v_m	1678.0	1838.1

Figure captions

Figure 1. (**Color online**) Cubic unit cell of As_4O_6 (a) and $As_4O_6 \cdot 2He$ (b). Grey (big), red (medium) and blue(small) balls correspond to As, O and He atoms, respectively.

Figure 2. (**Color online**) (a) Raman spectra of As_4O_6 up to 21 GPa when pressurized with a 4:1 methanol-ethanol mixture. (b) Pressure dependence of the experimental (symbols) and theoretical (solid lines) Raman-mode frequencies. The theoretical T_{1g}^1 (T_{2u}^1) inactive mode is shown with a dotted (dash-dotted) line. Pink symbols represent the extra Raman modes observed or used to fit the profile of broadened asymmetric peaks on increasing pressure.

Figure 3. (**Color online**) (a) Detail of the Raman spectra of As_4O_6 up to 12 GPa when pressurized without any pressure-transmitting medium. (b) Pressure dependence of the experimental (symbols) and theoretical (solid lines) Raman-mode frequencies. The theoretical T_{1g}^1 inactive mode is shown with a dashed line. Pink symbols represent the extra Raman modes observed or used to fit the profile of asymmetric peaks.

Figure 4. (**Color online**) (a) Raman spectra of As_4O_6 up to 3 GPa and of $As_4O_6 \cdot 2He$ from 3 GPa up to 14 GPa. (b) Pressure dependence of the experimental (full symbols) and theoretical (dash-dotted lines) Raman-mode frequencies of $As_4O_6 \cdot 2He$. Experimental Raman-mode frequencies for As_4O_6 up to 3 GPa are shown with empty symbols. Theoretical data for As_4O_6 (solid lines) are also shown for comparison with those of $As_4O_6 \cdot 2He$ to note the effect of He entrance in 16d sites of As_4O_6. The theoretical T_{1g}^1 inactive mode is shown in pink with a dashed line for As_4O_6 and with a dotted line for $As_4O_6 \cdot 2He$. Pink symbols represent the extra Raman modes observed or used to fit the profile of asymmetric peaks.

Figure 5. Phonon dispersion curves of As_4O_6 at 0 GPa (a) and 34.7 GPa (b).

Figure 6. Phonon dispersion curves of $As_4O_6 \cdot 2He$ at 5.2 GPa (a) and 35.5 GPa (b).

Figure 7. (**Color online**) Pressure dependence of the theoretical elastic constants (a) and elastic stiffness coefficients (b) in As_4O_6 and $As_4O_6 \cdot 2He$.

Figure 8. (Color online) Pressure dependence of the elastic moduli B_H, G_H, and E_H in As_4O_6 and $As_4O_6 \cdot 2He$.

Figure 9. Pressure dependence of the Poisson's ratio (ν_H), B_H/G_H ratio, and Zener anisotropy factor (A), in As_4O_6 and $As_4O_6 \cdot 2He$.

Figure 10. Evolution with pressure of the Vickers hardness in As_4O_6 and $As_4O_6 \cdot 2He$.

Figure 11. (Color online) Pressure dependence of the longitudinal (v_{lon}), transverse (v_{trans}), and average (v_m) elastic wave velocity in As_4O_6 and $As_4O_6 \cdot 2He$.

Figure 12. (**Color online**) General stability criteria in As_4O_6 and $As_4O_6 \cdot 2He$. The pressure at which As_4O_6 becomes mechanically unstable is indicated.

Figure 1

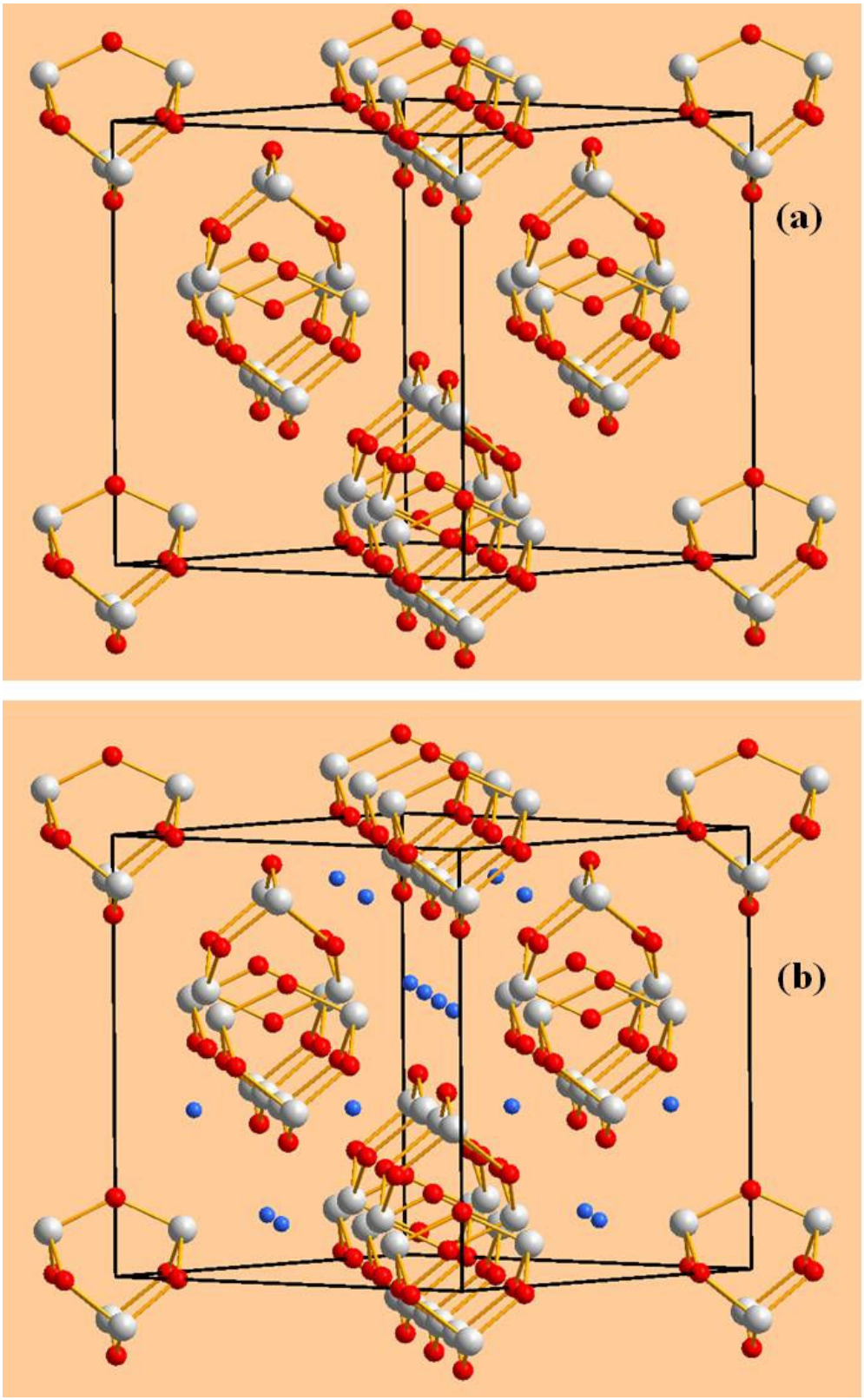

Figure 2

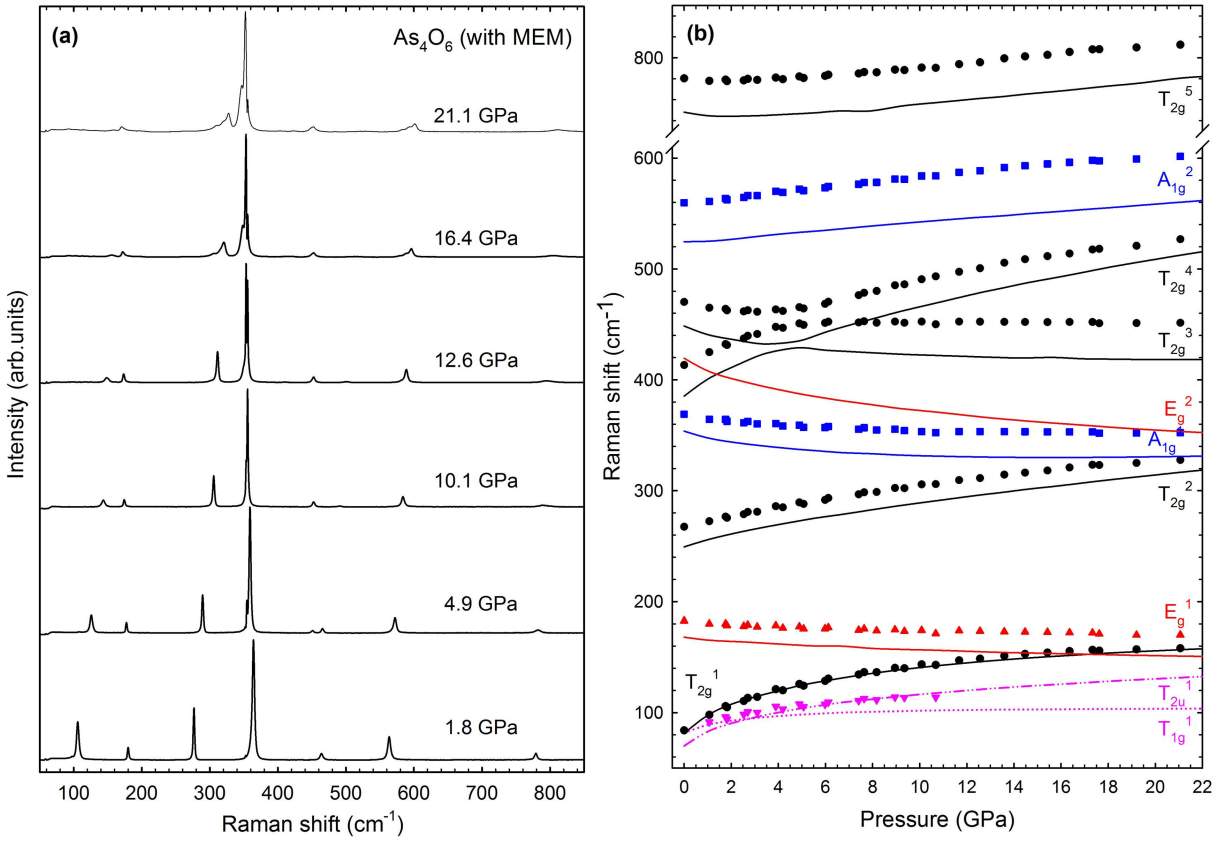
(a)
As4O6 (with MEM)
21.1 GPa
16.4 GPa
12.6 GPa
10.1 GPa
4.9 GPa
1.8 GPa
Intensity (arb.units)
Raman shift (cm-1)
(b)
Raman shift (cm-1)
Pressure (GPa)
T2g 5
A1g 2
T2g 4
T2g 3
Eg 2
A1g
T2g 2
Eg 1
T2g 1
T2u 1
T1g 1

-

Figure 3

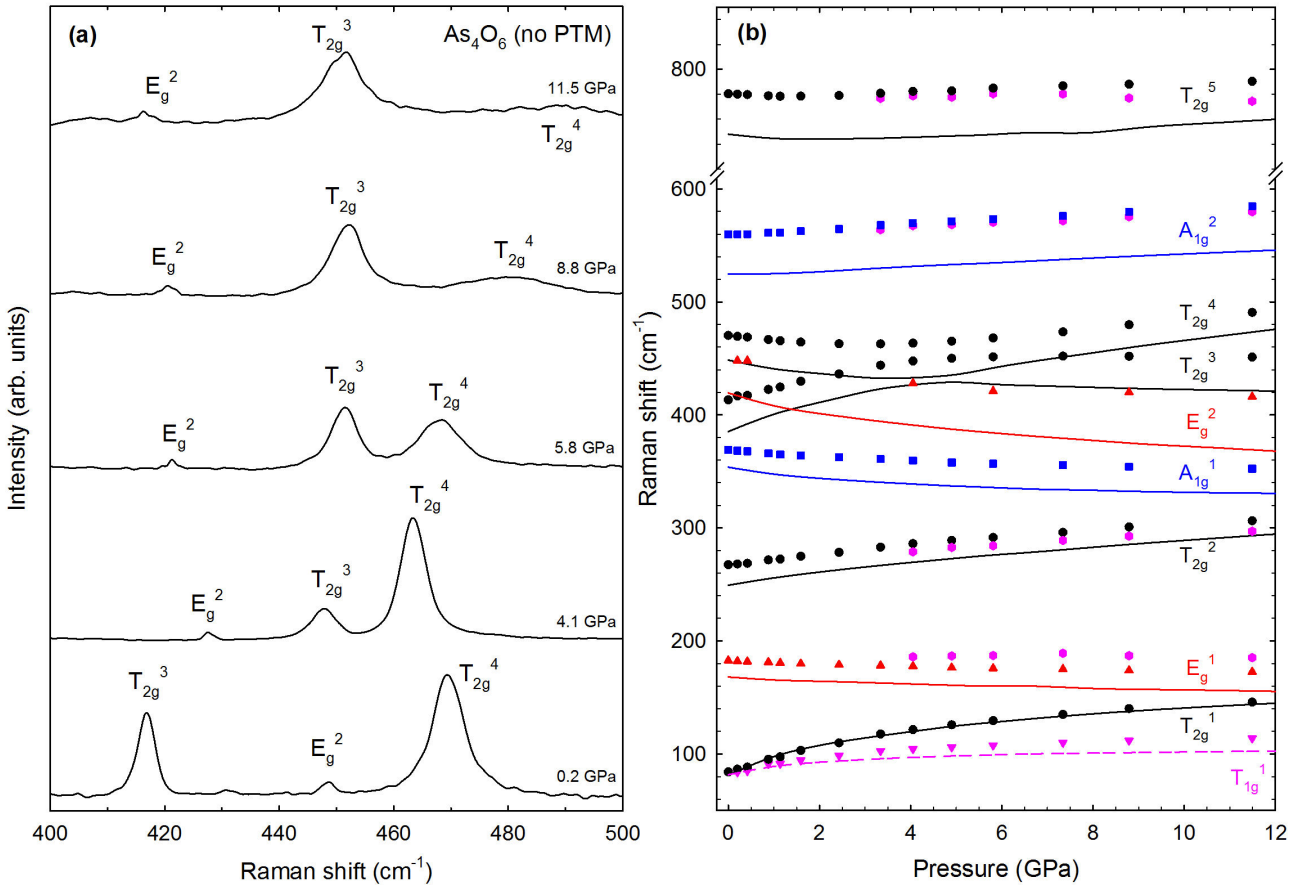
(a)
As4O6 (no PTM)
11.5 GPa
8.8 GPa
5.8 GPa
4.1 GPa
0.2 GPa
Intensity (arb. units)
Raman shift (cm-1)
(b)
Raman shift (cm-1)
Pressure (GPa)

Figure 4

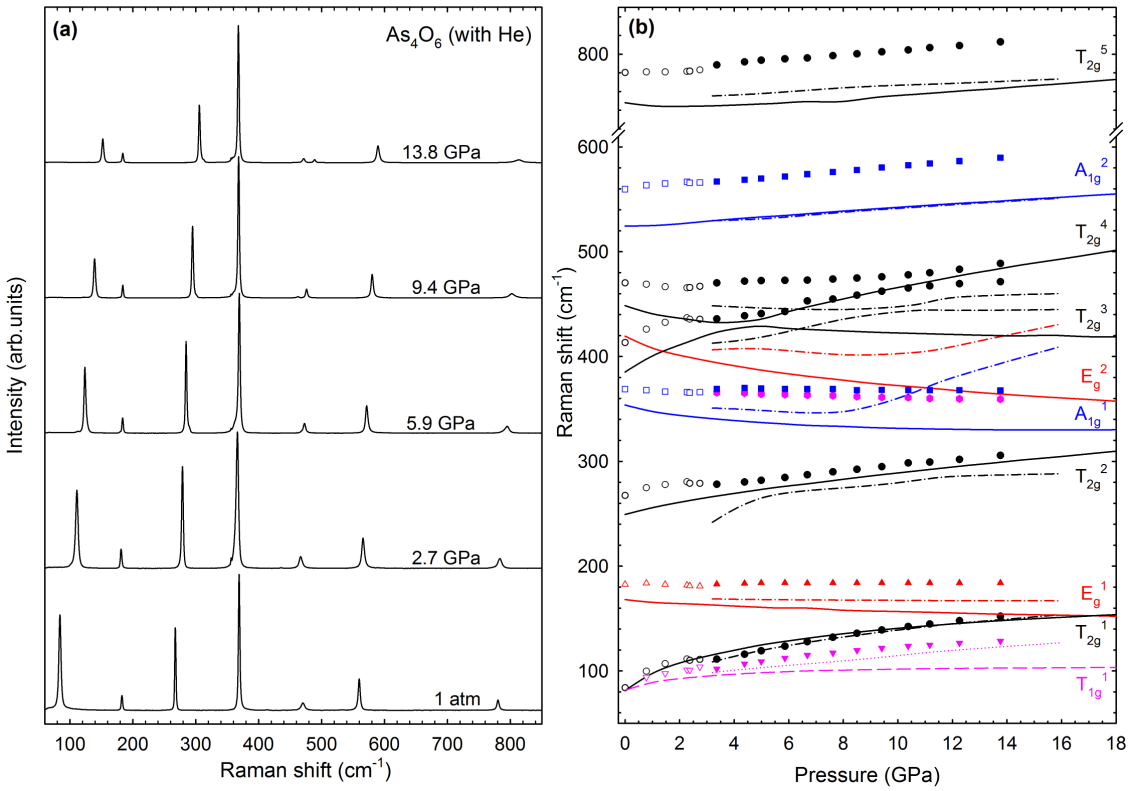
(a)
As4O6 (with He)
13.8 GPa
9.4 GPa
5.9 GPa
2.7 GPa
1 atm
Intensity (arb.units)
Raman shift (cm-1)
(b)
T2g5
A1g2
T2g4
T2g3
Eg2
A1g1
T2g2
Eg1
T2g1
T1g1
Raman shift (cm-1)
Pressure (GPa)

Figure 5

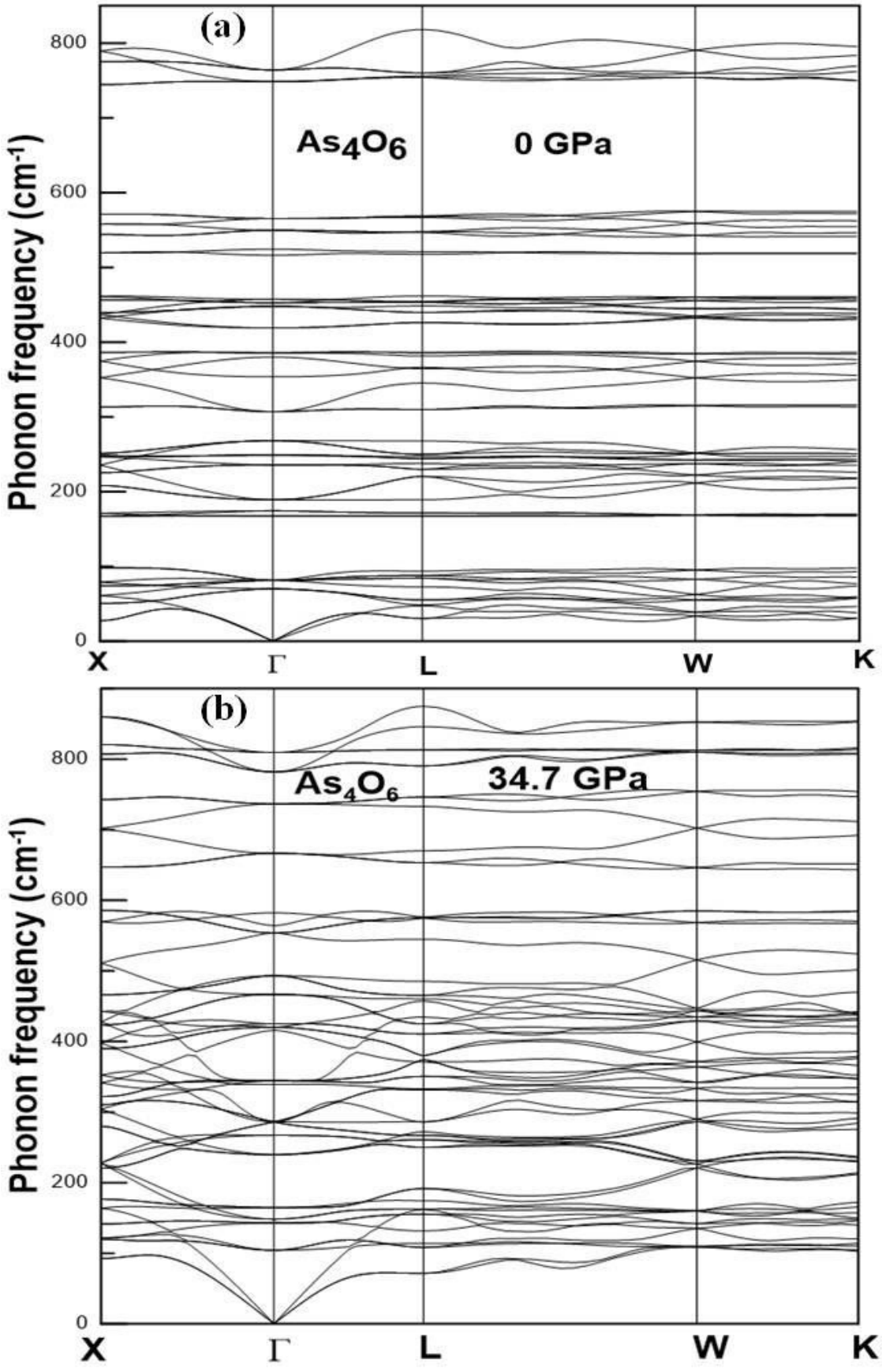
(a)
As4O6
0 GPa
Phonon frequency (cm-1)
800
600
400
200
0
X
Γ
L
W
K
(b)
As4O6
34.7 GPa
Phonon frequency (cm-1)
800
600
400
200
0
X
Γ
L
W
K

Figure 6

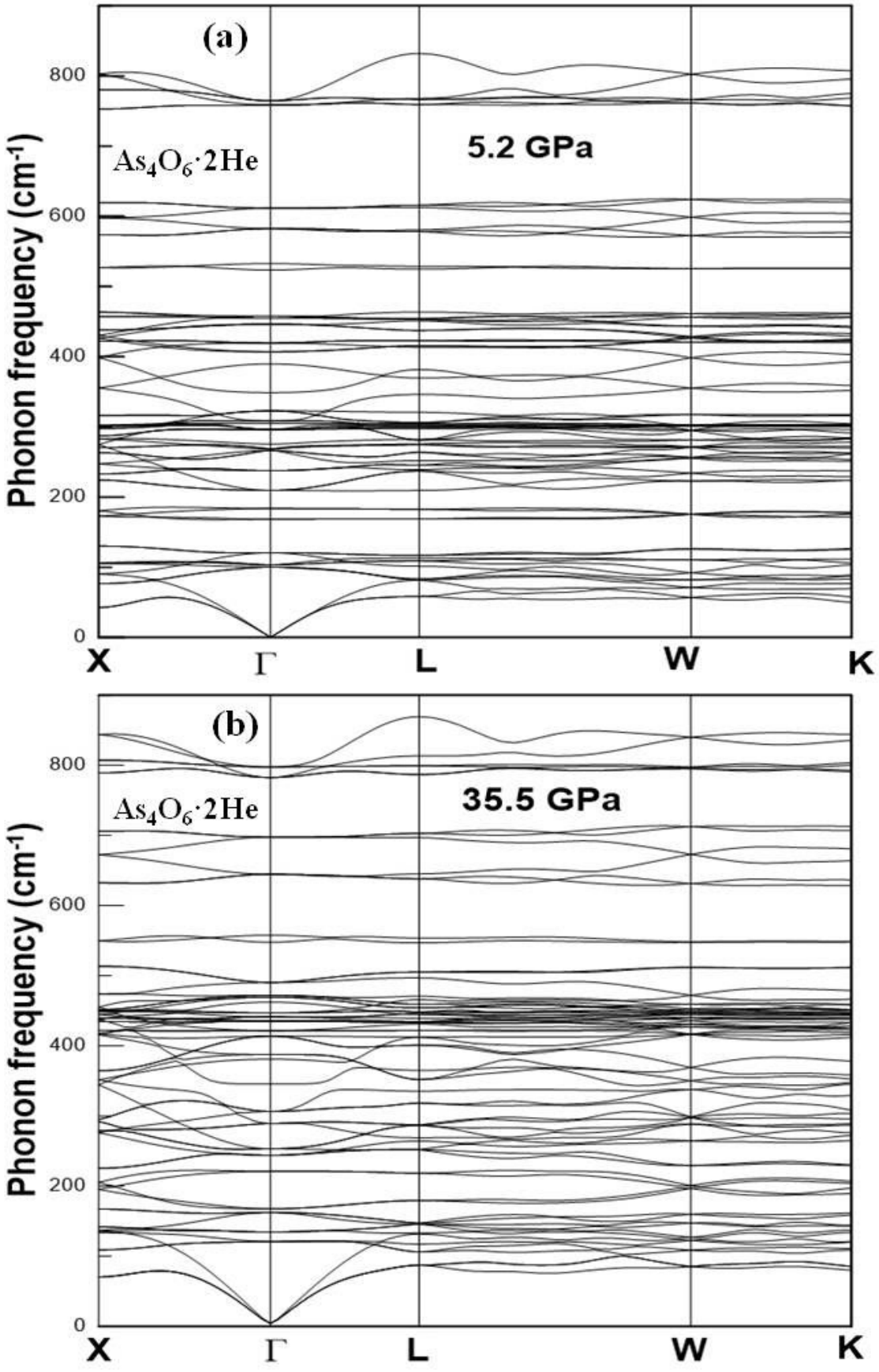
(a)
5.2 GPa
As4O6·2He
Phonon frequency (cm-1)
800
600
400
200
0
X
Γ
L
W
K
(b)
35.5 GPa
As4O6·2He
Phonon frequency (cm-1)
800
600
400
200
0
X
Γ
L
W
K

Figure 7

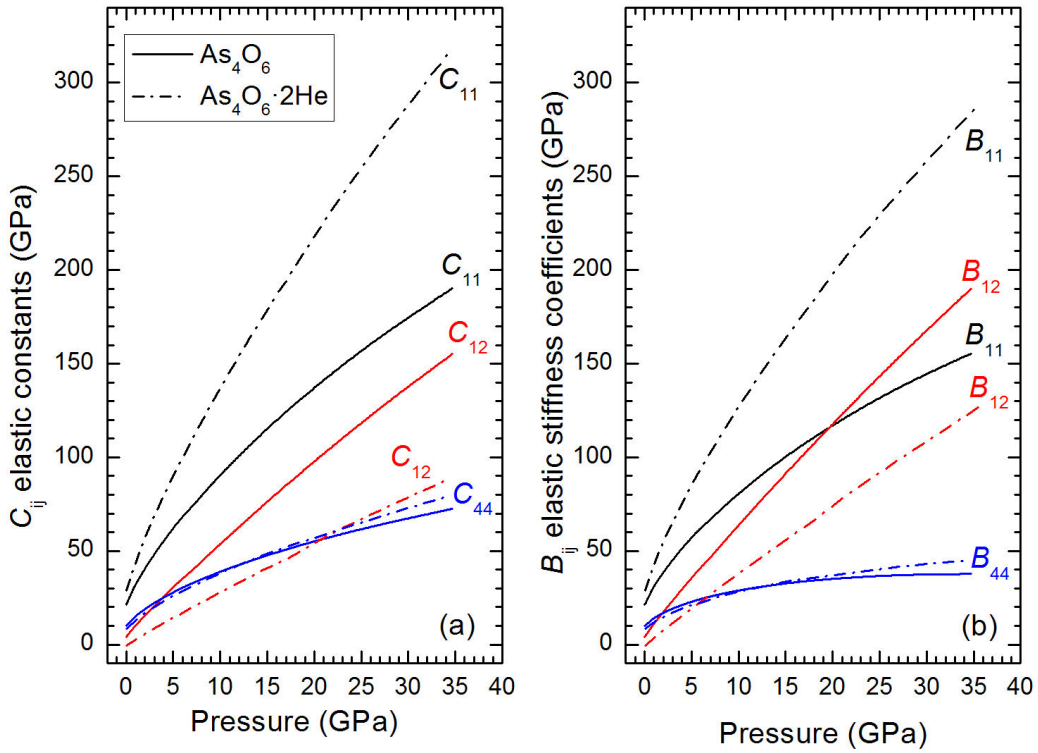
As4O6
As4O6·2He
C11
C11
C12
C12
C44
(a)
Cij elastic constants (GPa)
Pressure (GPa)
B11
B12
B11
B12
B44
(b)
Bij elastic stiffness coefficients (GPa)
Pressure (GPa)

Figure 8

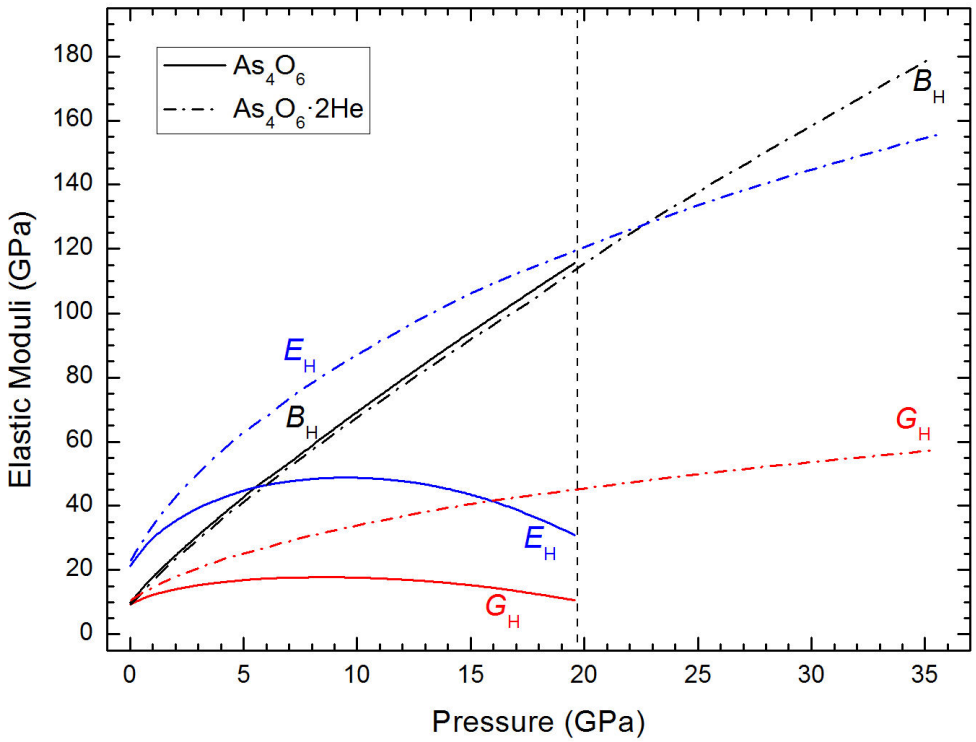
As4O6
As4O6·2He
Elastic Moduli (GPa)
Pressure (GPa)
0
20
40
60
80
100
120
140
160
180
0
5
10
15
20
25
30
35
BH
EH
BH
GH
EH
GH

Figure 9

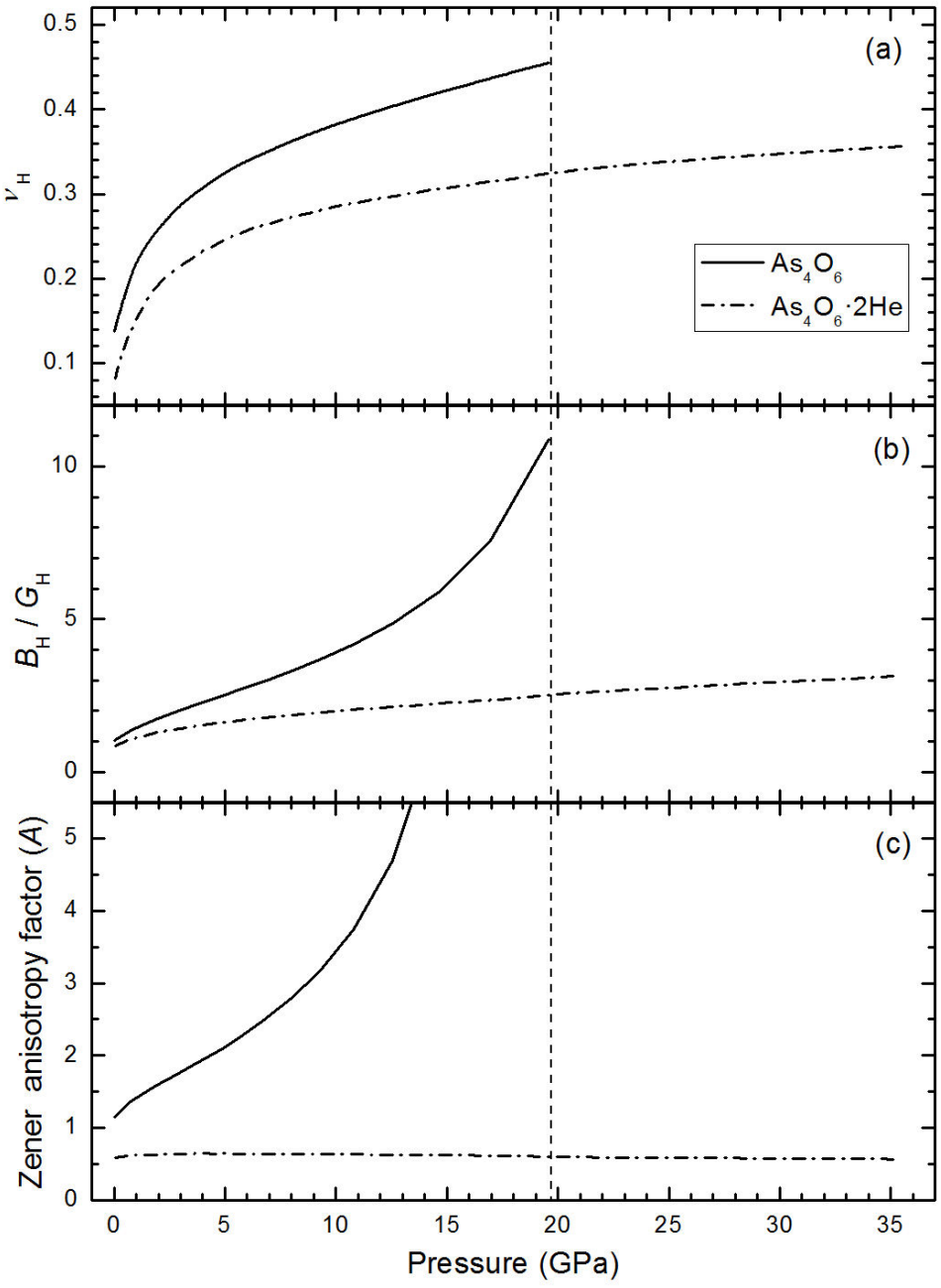
(a)
(b)
(c)
ν_H
B_H / G_H
Zener anisotropy factor (A)
As_4O_6
$As_4O_6 \cdot 2He$
Pressure (GPa)
0.1
0.2
0.3
0.4
0.5
0
5
10
15
20
25
30
35
1
2
3
4

Figure 10

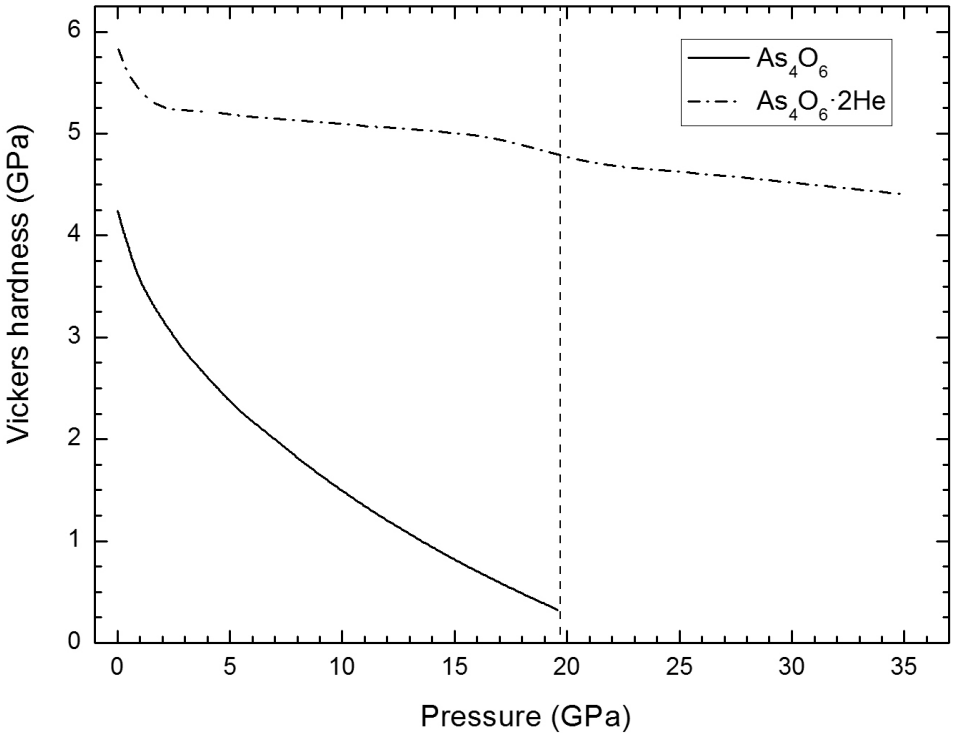
Vickers hardness (GPa)
Pressure (GPa)
As4O6
As4O6·2He
0
1
2
3
4
5
6
0
5
10
15
20
25
30
35

Figure 11

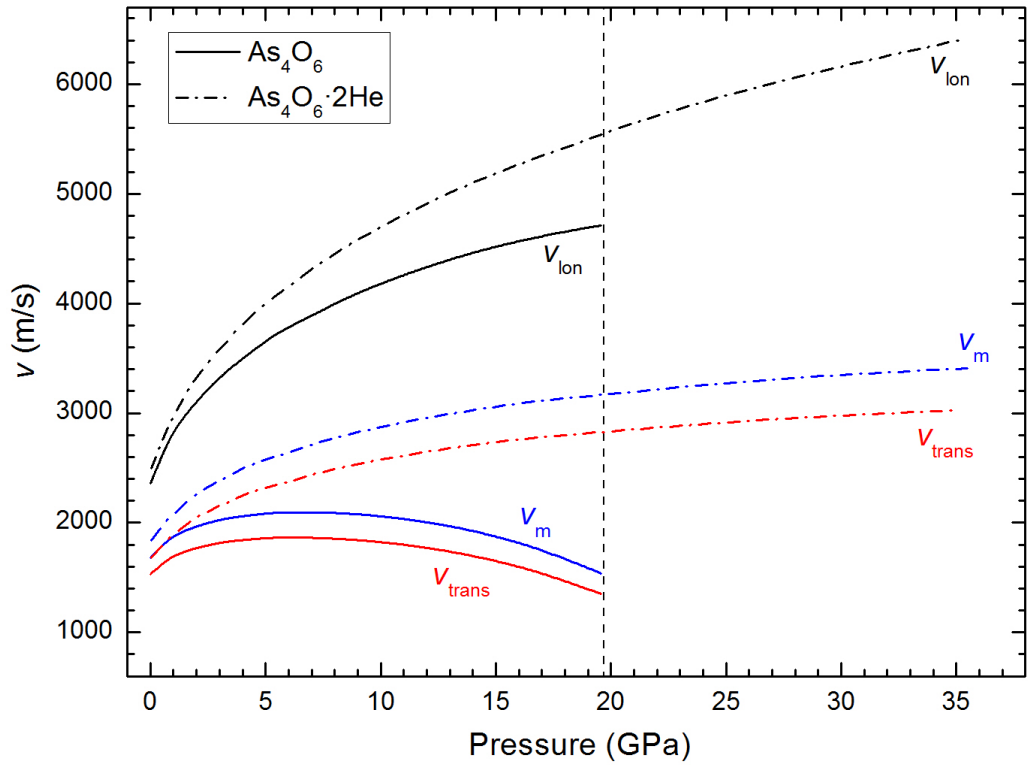
As4O6
As4O6·2He
v (m/s)
Pressure (GPa)
V lon
V lon
V m
V m
V trans
V trans
6000
5000
4000
3000
2000
1000
0
5
10
15
20
25
30
35

Figure 12

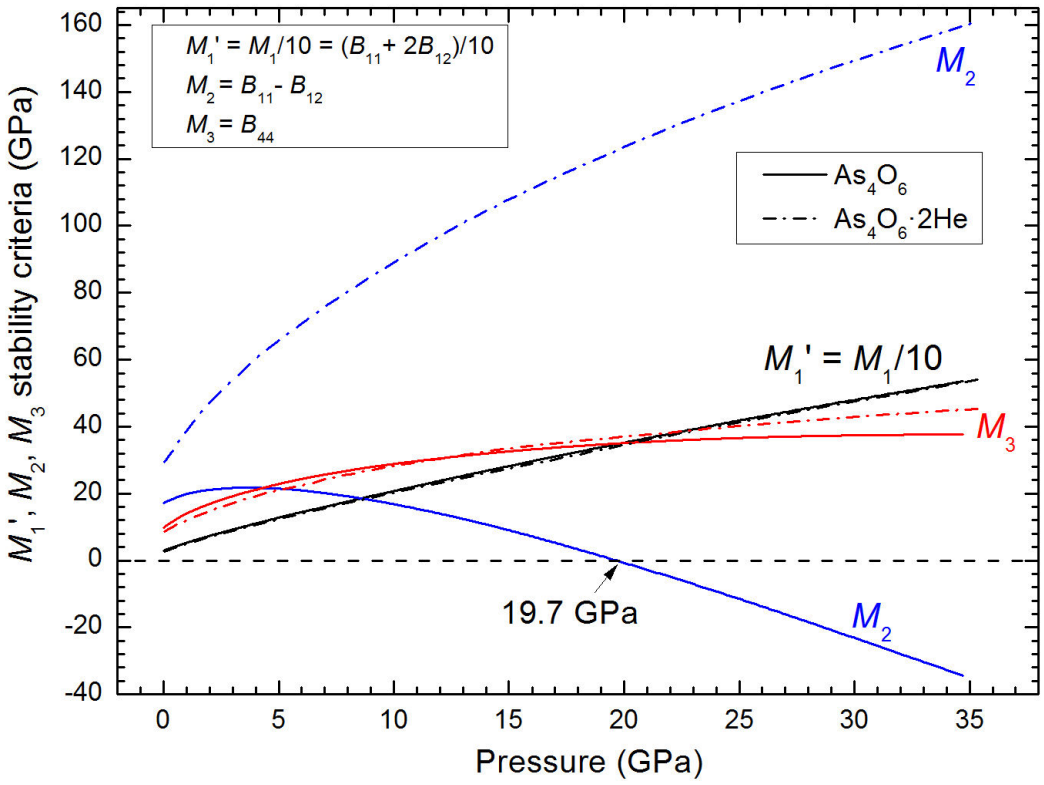
$M_1' = M_1/10 = (B_{11} + 2B_{12})/10$
$M_2 = B_{11} - B_{12}$
$M_3 = B_{44}$
As_4O_6
$As_4O_6 \cdot 2He$
M_2
$M_1' = M_1/10$
M_3
19.7 GPa
M_2
M_1', M_2, M_3 stability criteria (GPa)
Pressure (GPa)
160
140
120
100
80
60
40
20
0
-20
-40
0
5
10
15
20
25
30
35

Supplementary material of

Vibrational and elastic properties of As_4O_6 and $As_4O_6 \cdot 2He$ at high pressures: Study of dynamical and mechanical stability

V.P. Cuenca-Gotor,[1] O. Gomis,[2,a)] J.A. Sans,[1] F. J. Manjón,[1]
P. Rodríguez-Hernández,[3] and A. Muñoz [3]

[1] Instituto de Diseño para la Fabricación y Producción Automatizada, MALTA Consolider Team, Universitat Politècnica de València, 46022 València, Spain

[2] Centro de Tecnologías Físicas: Acústica, Materiales y Astrofísica, MALTA Consolider Team, Universitat Politècnica de València, 46022 València, Spain

[3] Departamento de Física, Instituto de Materiales y Nanotecnología, MALTA Consolider Team, Universidad de La Laguna, 38205 Tenerife, Spain

a) Author to whom correspondence should be addressed. Electronic mail: osgohi@fis.upv.es

A. Lattice dynamics

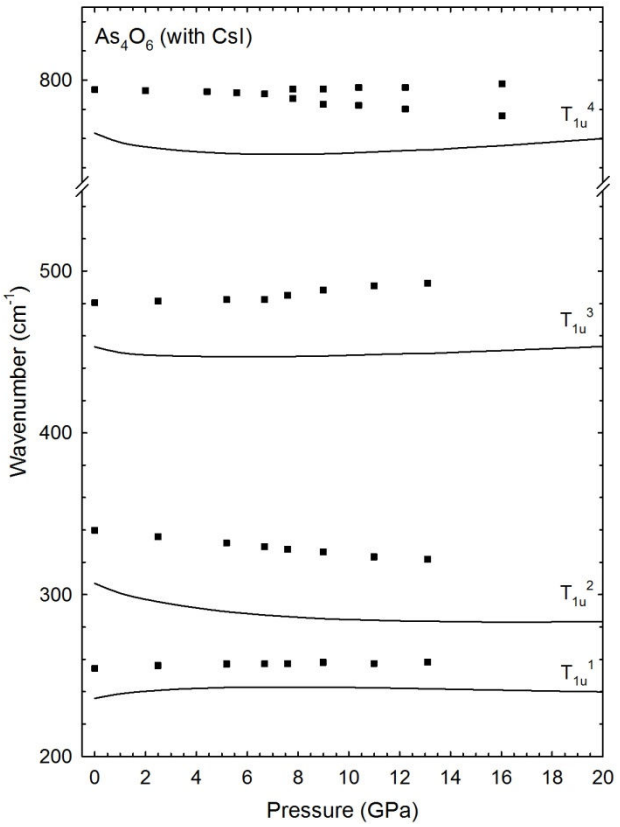

Figure S1. Experimental and theoretical pressure dependence of the IR-active modes in As_4O_6. Experimental data measured using CsI as a PTM are taken from Ref. S1.

Table SI. Theoretical and experimental zero-pressure frequencies and pressure coefficients of IR-active modes in As_4O_6 at 0 GPa. Experimental data are taken from Ref. S1.

	Ab initio calculations		Experimental	
Mode (Sym)	ω_0 (cm^{-1})	$\frac{\partial\omega}{\partial P}$ $\left(\frac{cm^{-1}}{GPa}\right)$	ω_0 (cm^{-1})	$\frac{\partial\omega}{\partial P}$ $\left(\frac{cm^{-1}}{GPa}\right)$
T_{1u}^{1} (IR)	236.0	2.7	254.5	0.8
T_{1u}^{2} (IR)	306.7	-5.7	339.8	-1.5
T_{1u}^{3} (IR)	453.1	-3.8	480.4	0.1
T_{1u}^{4} (IR)	763.5	-6.6	793.4	-0.2

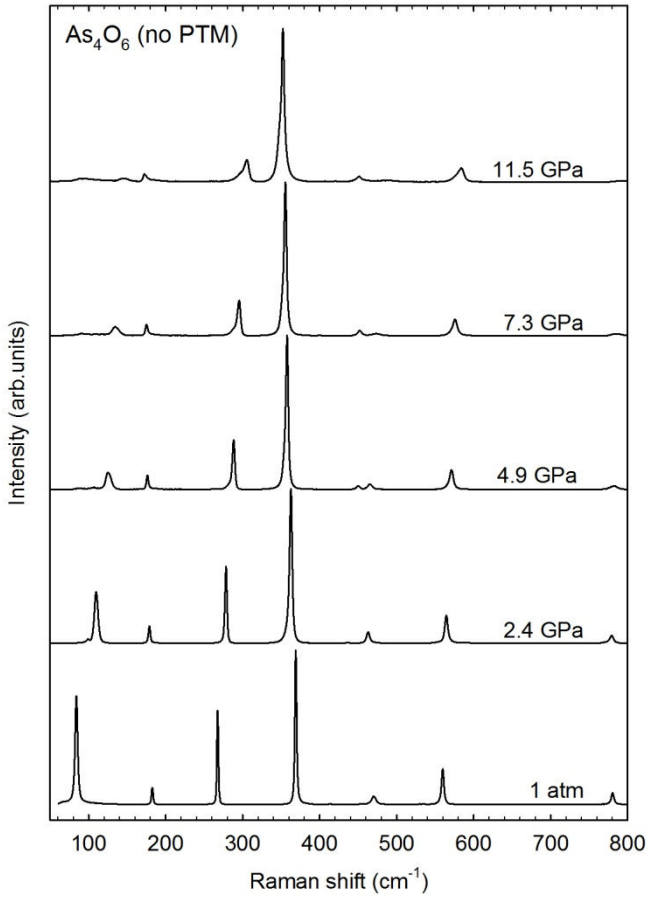

Figure S2. Raman scattering spectra of arsenolite at selected pressures without any PTM. Raman spectra are vertically shifted for the sake of clarity.

A progressive shift of the Raman-active mode frequencies of all peaks of the cubic structure with increasing pressure is observed in As_4O_6 compressed without any PTM. Absence of new peaks at high pressure clearly indicates that no phase transition occurs along the pressure range studied. Many Raman modes undergo a progressive asymmetric broadening with increasing pressure. This broadening is likely caused by the increase of intermolecular interactions; i.e., the increase of interactions among As_4O_6 cages, which finally results in the onset of PIA above 15 GPa.

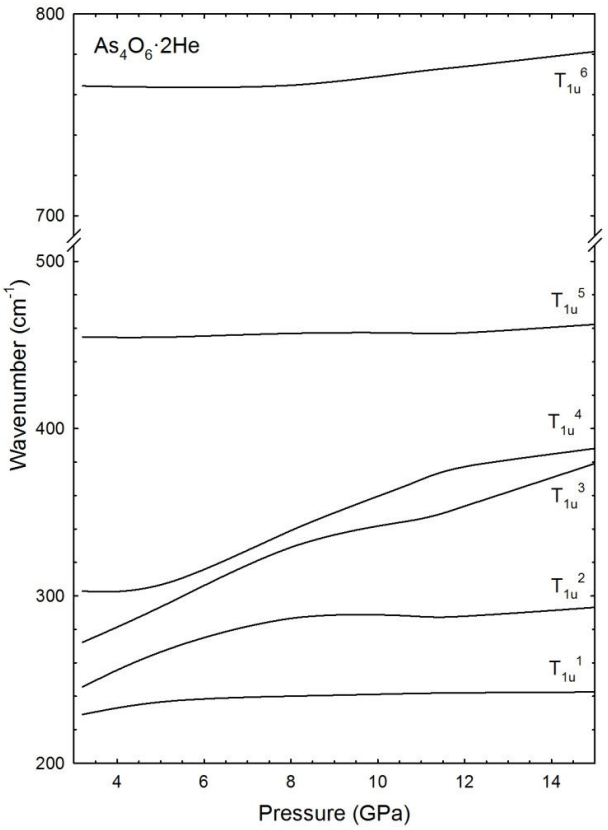

Figure S3. Theoretical pressure dependence of the IR-active modes in $As_4O_6 \cdot 2He$.

There are two additional IR-active modes in $As_4O_6 \cdot 2He$ than in As_4O_6. The two extra modes are located between the two lowermost IR-active modes of As_4O_6 and have a much larger pressure coefficient than IR-active modes of As_4O_6 thus leading to anticrossings with the mode above 300 cm^{-1}.

Table SII. Theoretical frequencies and pressure coefficients of IR-active modes in $As_4O_6 \cdot 2He$ at 3 GPa.

	Ab initio calculations	
Mode (Sym)	ω_0 (cm^{-1})	$\frac{\partial\omega}{\partial P}$ $\left(\frac{cm^{-1}}{GPa}\right)$
T_{1u}^{1}	230.0	3.3
T_{1u}^{2}	247.5	11.2
T_{1u}^{3}	271.6	12.5
T_{1u}^{4}	300.3	0.3
T_{1u}^{5}	455.1	-0.7
T_{1u}^{6}	763.8	-1.1

B. Thermodynamic properties

The Debye temperature is a fundamental parameter that correlates with many physical properties of solids, such as specific heat, elastic constants, and melting temperature. One of the standard methods to calculate the Debye temperature, θ_D, is from elastic constant data using the semi-empirical formula **[S2]**:

$$\theta_D = \frac{h}{k_B}\left[\frac{3n}{4\pi}\left(\frac{N_A\rho}{M}\right)\right]^{1/3} v_m$$

where h is the Planck's constant, k_B is the Boltzmann's constant, n is the number of atoms in the molecule, N_A is the Avogadro's number, ρ is the density, M is the molecular weight, and v_m is the averaged sound velocity. As reported in **Table SIII**, the values of θ_D at 0 GPa using the Hill approximation are 196.2 K (222.7 K) in As_4O_6 ($As_4O_6{\cdot}2He$). We note that the Debye temperature in $As_4O_6{\cdot}2He$ is slightly greater than that of As_4O_6. **Figure S4(a)** reports the evolution with pressure of the Debye temperature, θ_D, for both oxides. It is observed that θ_D follows a similar dependence than v_m with increasing pressure; i.e., increases at low pressures in both oxides and decreases above 8 GPa in As_4O_6 while it increases in $As_4O_6{\cdot}2He$ at least up to 35 GPa.

The thermal conductivity is the property of a material that indicates its ability to conduct heat. In order to estimate the theoretical minimum of the thermal conductivity, we have used the following expression **[S3]**:

$$\kappa_{\min} = k_B v_m \left(\frac{M}{n\rho N_A}\right)^{-2/3}$$

The values of κ_{min} in As_4O_6 ($As_4O_6{\cdot}2He$) at 0 GPa using the Hill approximation are 0.36 (0.42) W m^{-1} K^{-1} (see **Table SIII**). Therefore, both oxides are low κ materials **[S4]. Figure S4(b)** reports the evolution with pressure of the minimum thermal conductivity, κ_{min}, for both oxides. As in the case of θ_D, κ_{min} first increases with pressure and latter it decreases with pressure because of the decreasing of v_m with pressure for As_4O_6, while κ_{min} increases with pressure up to 35 GPa in $As_4O_6{\cdot}2He$. On the other hand, if we use the simplified formula for κ_{min} that considers $v_m = 0.87\sqrt{E/\rho}$

[S3], the decreasing of κ_{min} with pressure in As_4O_6 can be explained by the decreasing of the tensile stiffness of As_4O_6 as pressure increases above 9 GPa.

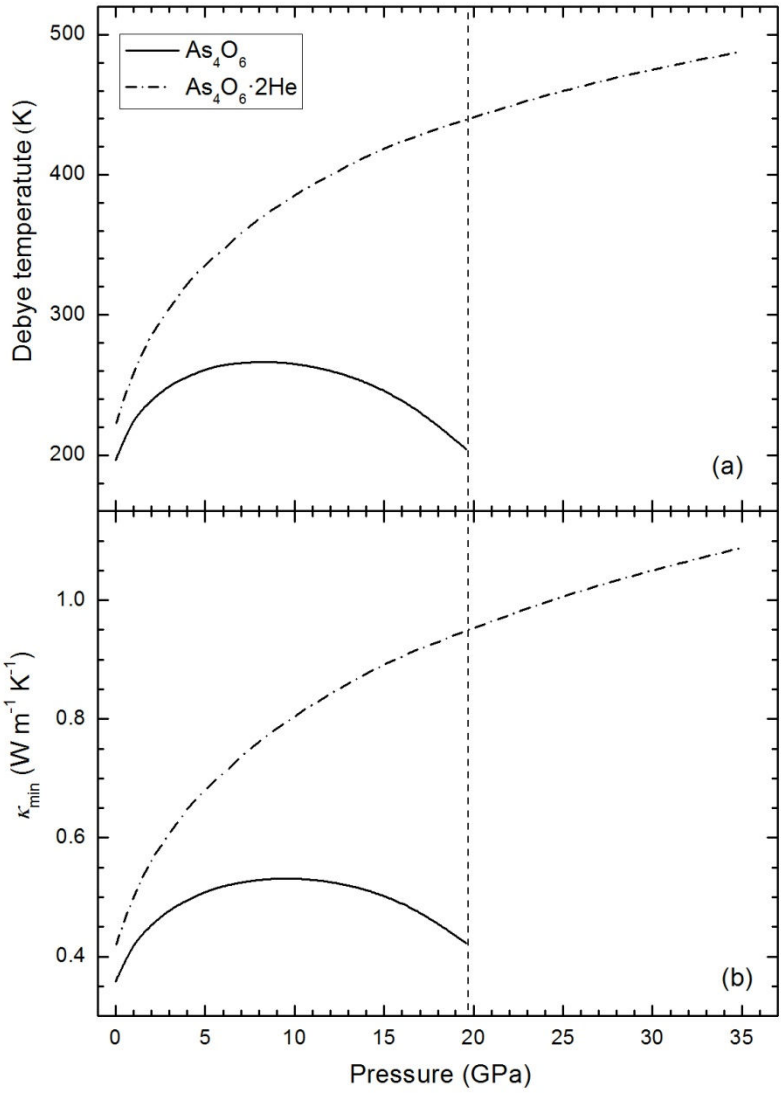

Figure S4. Evolution with pressure of the theoretical Debye temperature (a) and theoretical minimum thermal conductivity, κ_{min}, (b) in As_4O_6 and $As_4O_6 \cdot 2He$.

Table SIII. Debye temperature (θ_D in K), and minimum thermal conductivity (κ_{min} in W m^{-1} K^{-1}) in As_4O_6 and $As_4O_6 \cdot 2He$ at 0 GPa. Data are given in the Hill approximation.

	As_4O_6	$As_4O_6 \cdot 2He$
θ_D	196.2	222.7
κ_{min}	0.36	0.42

References

[S1] A. Grzechnik, J. Solid State Chem. 144, 416 (1999).

[S2] O. L. Anderson, J. Phys. Chem. Solids 24, 909-917 (1963).

[S3] D. R. Clarke, Surf. Coat. Technol. 163, 67-74 (2003).

[S4] C. G. Levi, Curr. Opin. Solid State Matter. Sci. 8, 77-91 (2004).